communications biology

Article

https://doi.org/10.1038/s42003-024-07344-6

Abnormal cytoskeletal remodeling but normal neuronal excitability in a mouse model of the recurrent developmental and epileptic encephalopathy-susceptibility KCNB1-p.R312H variant

Alessandro Bortolami[1], Elena Forzisi Kathera-Ibarra[1], Anastasia Balatsky[1], Mansi Dubey[1], Rusheel Amin[1], Srinidi Venkateswaran[1], Stefania Dutto[1], Ishan Seth[1], Adam Ashor[1,2], Angel Nwandiko[1], Ping-Yue Pan[1], David P. Crockett[1] & Federico Sesti[1]

Integrin_K^+ Channel_Complexes (IKCs), are implicated in neurodevelopment and cause developmental and epileptic encephalopathy (DEE) through mechanisms that were poorly understood. Here, we investigate the function of neocortical IKCs formed by voltage-gated potassium (Kv) channels Kcnb1 and α5β5 integrin dimers in wild-type (WT) and homozygous knock-in (KI) *Kcnb1*$^{R312H(+/+)}$ mouse model of DEE. *Kcnb1*$^{R312H(+/+)}$ mice suffer from severe cognitive deficit and compulsive behavior. Their brains show neuronal damage in multiple areas and disrupted corticocortical and corticothalamic connectivity along with aberrant glutamatergic vesicular transport. Surprisingly, the electrical properties of *Kcnb1*$^{R312H(+/+)}$ pyramidal neurons are similar to those of WT neurons, indicating that the arginine to histidine replacement does not affect the conducting properties of the mutant channel. In contrast, fluorescence recovery after photobleaching, biochemistry, and immunofluorescence, reveal marked differences in the way WT and *Kcnb1*$^{R312H(+/+)}$ neurons modulate the remodeling of the actin cytoskeleton, a key player in the processes underlying neurodevelopment. Together these results demonstrate that Kv channels can cause multiple conditions, including epileptic seizures, through mechanisms that do not involve their conducting functions and put forward the idea that the etiology of DEE may be primarily non-ionic.

Building evidence indicates that voltage-gated potassium (Kv) channels are not isolated entities in the plasma membrane but rather key elements of broader networks of interacting proteins. An example in this sense is provided by the Kv channel Kcnb1. The channel is widely expressed in the brain where it mediates an important delayed rectifier potassium (K^+) current. Like other Kv channels, Kcnb1 forms stable complexes with integrins, named Integrin_K^+ Channel_Complexes or IKCs[1]. These IKCs modulate both the migration of glutamatergic excitatory neurons to the upper neocortical layers (UL) during neurodevelopment and their excitability[2,3]. Furthermore, the *KCNB1* gene is implicated in developmental and epileptic encephalopathy (DEE), an umbrella term to describe a group of conditions in which severe developmental delay is often associated with infant epilepsy characterized by seizures, often drug-resistant, and abundant epileptiform activity[4]. To date, more than 50 *KCNB1* pathogenic variants have been discovered in children with DEE[5–7]. The clinical manifestations of *KCNB1* mutations vary: all patients have developmental encephalopathy and the majority (~80%) experience seizures. Roughly 30% of those patients also present brain anomalies that may include white matter malformations, brain atrophy, cerebellar volume loss, and abnormal corpus callosum[5,8,9]. Notably, clinical cases of patients having brain anomalies with mild phenotype and no seizures are also documented[8,10,11]. Even though the etiology of DEE is typically monogenic, the epilepsy and the encephalopathy develop

[1]Department of Neuroscience and Cell Biology, Robert Wood Johnson Medical School, Rutgers University, Piscataway, NJ, USA. [2]Present address: Nilo Therapeutics, New York, NY, USA. e-mail: federico.sesti@rutgers.edu

independently of each other[12,13]. This highlights one challenge in DEE research: to decipher how a single gene can simultaneously cause multiple conditions. The discovery of the IKC can provide an answer to this conundrum as an aberrant IKC has the potential to cause both epilepsy and developmental encephalopathy, presumably via electrical (ionic) and non-electrical (non-ionic) mechanisms. In this study, we analyze the properties of IKCs expressed in the brains of wild-type (WT) mice and of a homozygous *Knock in* (KI) mouse model of DEE harboring the $Kcnb1^{R312H}$ allele[2]. We show that the latter animals present broad cognitive impairment and brain malformations, that along with the epilepsy reported previously, are reminiscent of the human DEE phenotype. At the molecular level, the IKC modulates the remodeling of the actin cytoskeleton, a major substrate of integrins and a key element in many neurodevelopmental mechanisms. Remarkably, the electrical properties of primary pyramidal $Kcnb1^{R312H(+/+)}$ neurons are normal. Together this suggests, that a defective IKC can cause multiple conditions, including epileptic seizures, via mechanisms that do not depend on its conducting functions.

Results

$Kcnb1^{R312H(+/+)}$ mice exhibit developmental encephalopathy-like traits

We monitored the mice in a non-invasive manner, using the Digital Ventilated Cage (DVC) system, which continuously records the position of the animal in the cage using touchless sensors. Physical activity is minimal and comparable between WT and $Kcnb1^{R312H(+/+)}$ mice during the diurnal cycle, when the animals typically rest (Fig. 1A. The $Kcnb1^{R312H}$ mouse, bears a mutated allele that causes an arginine to histidine replacement in the S4 transmembrane segment). In contrast, $Kcnb1^{R312H(+/+)}$ mice are largely more active than WT mice during the nocturnal cycle. As the former animals are subject to spontaneous convulsive seizures, which may give rise to false readings, we computed the distance traveled per minute[2]. Distance per minute was minimal for WT and $Kcnb1^{R312H(+/+)}$ males and females over the daily hours and largely increased over the night (Fig. 1B). Overall $Kcnb1^{R312H(+/+)}$ mice traveled a cumulative distance roughly twice as much as WT mice over a week (Fig. 1C). In a second experiment we recorded the cumulative distance run on a wheel. In a week, WT male and female animals together run ~10 km. In contrast the $Kcnb1^{R312H(+/+)}$ animals run ~65 km, a 6-7-fold increase (Fig. 1D). We conclude that $Kcnb1^{R312H(+/+)}$ mice are physically hyperactive in agreement with other mouse models of DEE[14,15]. As DEE children present broad-spectrum developmental deficits, we next assessed several neurological functions in WT and $Kcnb1^{R312H(+/+)}$ animals, ranging from sensory perception and processing, to organized thinking. To this end, mice were subject to the nest building test, which gauges the general well-being of the animal and requires a significant amount of organized thinking; the marble burying test, which may reveal obsessive-compulsive traits; the path integration (dead reckoning) test, that determines the ability of the animal to construct mental maps of an unknown environment and return home without learned references; the visual looming test, that evaluates awareness to sudden dangers; the visual cliff that evaluates depth perception; the startle reflex test, that gauges response to sudden or threatening stimuli and the gait and hanging test, to measure muscular function[16–20]. Notably, $Kcnb1^{R312H(+/+)}$ mice performed significantly worse in all the tests compared to WT, revealing severe neurological dysfunction (Fig. 2). Even the poor performance of $Kcnb1^{R312H(+/+)}$ mice in the hanging test (Fig. 2G) is likely due to underlying neurological issues, for example depression—a common comorbidity of epilepsy—as those animals are

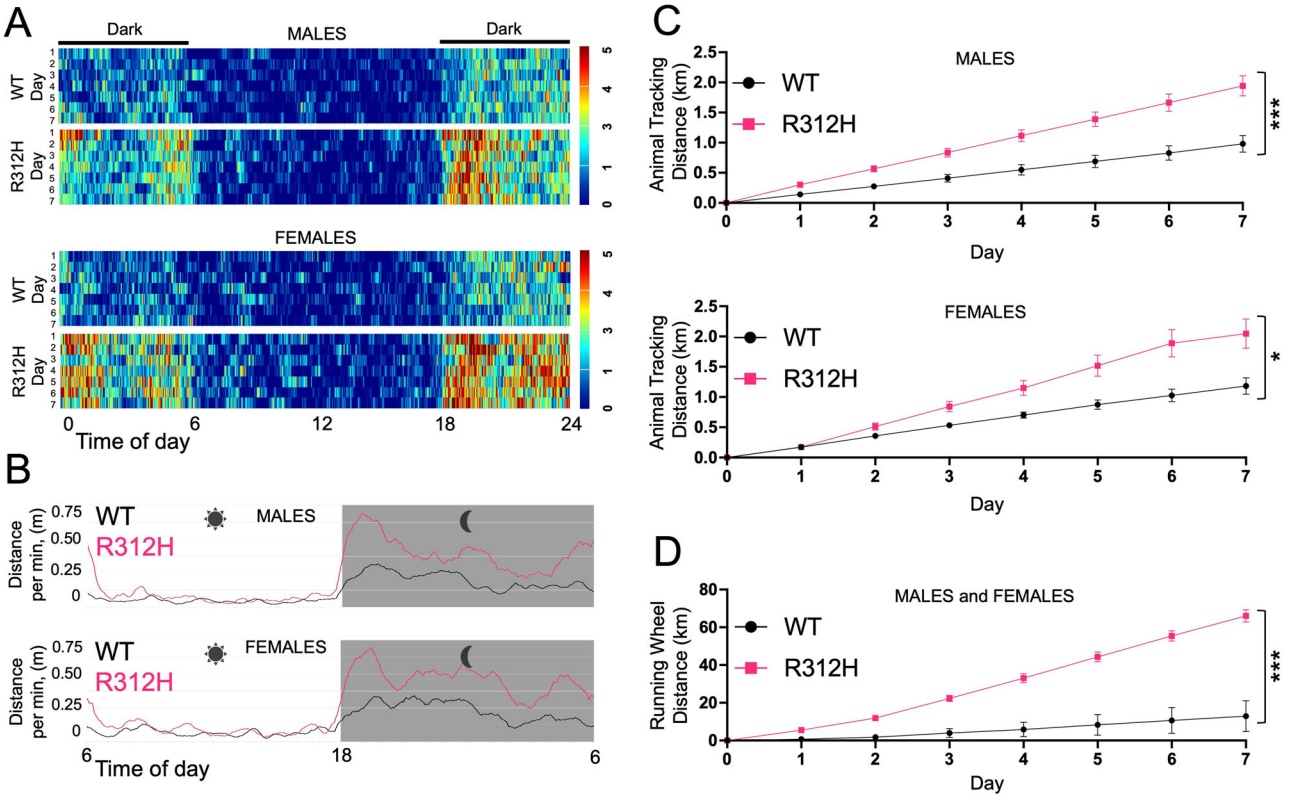

Fig. 1 | $Kcnb1^{R312H(+/+)}$ mice are hyperactive. A Heat maps showing 24 h of activity of single-housed WT and $Kcnb1^{R312H(+/+)}$ males and females. The period of major activity begins at ~ 18 h, when the light is turned off, and terminates at ~6 h, when the light is turned on. $N = 7$ mice/sex/genotype, recorded over a week. **B** Distance traveled per minute, during the day, averaged over a week for WT and $Kcnb1^{R312H(+/+)}$ males and females. $N = 28$ mice (seven males and seven females per genotype). **C** Cumulative daily distance traveled over a week by WT and $Kcnb1^{R312H(+/+)}$ males and females. $N = 28$ mice (seven males and seven females per genotype). **D** Cumulative distance run on the running wheel over a week by WT and $Kcnb1^{R312H(+/+)}$ males and females combined. $N = 5$ mice (three males and two females per genotype). In all experiments, three-month-old mice were used. There were no differences in size and body weight between WT and $Kcnb1^{R312H(+/+)}$ mice. $^{*}P < 0.05$, $^{***}P < 0.001$, two-tailed student's *t*-test.

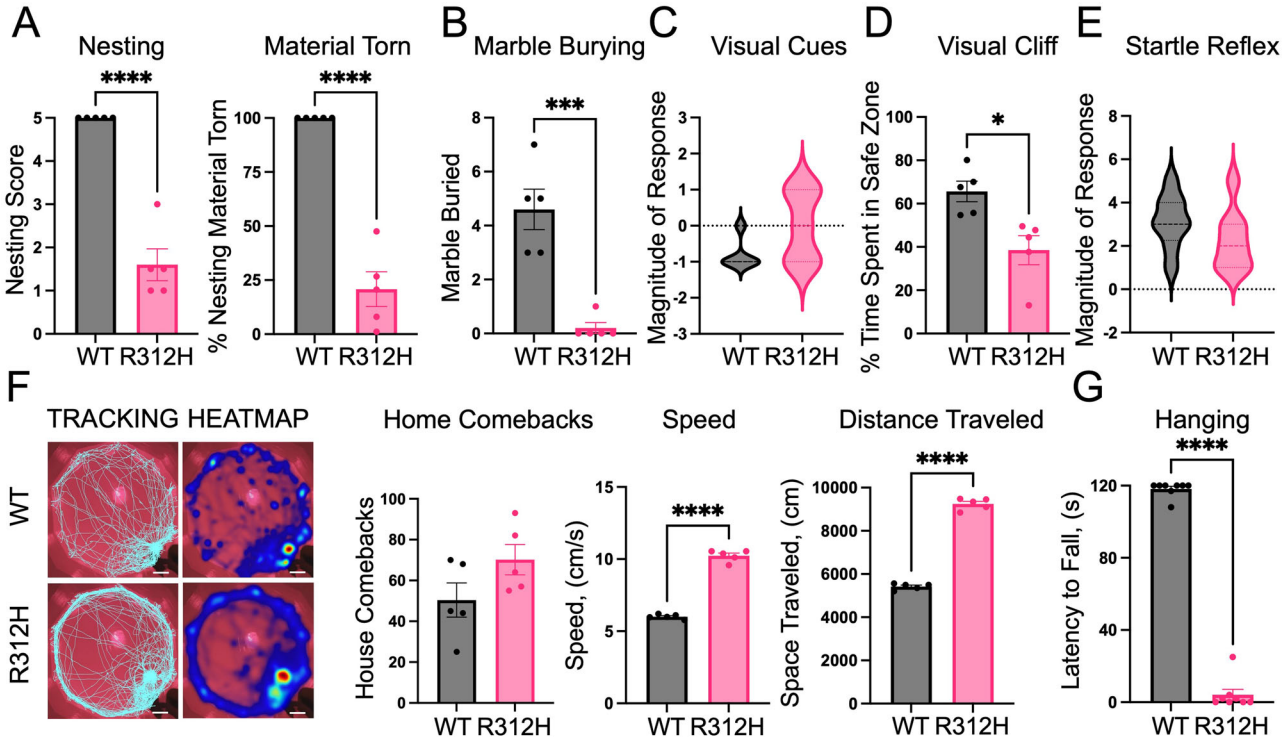

Fig. 2 | *Kcnb1*$^{R312H(+/+)}$ mice present severe cognitive impairment. A Percentage of nesting material used and nesting score (see methods) for WT and *Kcnb1*$^{R312H(+/+)}$ (R312H) mice. **B** Mean number of marbles buried by WT and *Kcnb1*$^{R312H(+/+)}$ mice. **C** Violin plot of the magnitude of response to a visual looming threat for WT and *Kcnb1*$^{R312H(+/+)}$ mice. $N = 5$ mice/genotype. **D** Time spent in the safe zone of the visual cliff arena for WT and *Kcnb1*$^{R312H(+/+)}$ mice. **E** Violin plot of the magnitude of response to a startling sound of WT and *Kcnb1*$^{R312H(+/+)}$ mice. $N = 8$ mice/genotype. **F** Representative heat maps of the distance traveled and quantifications of the comebacks to the house, mean speed, and distance traveled in the dead reckoning test by WT and *Kcnb1*$^{R312H(+/+)}$ mice. Scale bars 20 cm. **G** Latency to fall in the hanging test for WT and *Kcnb1*$^{R312H(+/+)}$ mice. In all behavioral tests, three-month-old mice were used. $^{*}P < 0.05$, $^{***}P < 0.001$, and $^{****}P < 0.0001$, two-tailed student's *t*-test.

physically hyperactive and their gait is normal. We reported previously that *Kcnb1*$^{R312H(+/+)}$ mice do not reproduce (they are obtained by breeding of heterozygous pairs), compulsively self-groom, and show high levels of anxiety[2]. In summary, the extensive neurological dysfunction of the *Kcnb1*$^{R312H(+/+)}$ mouse, along with hyperactivity and the severe seizure phenotype reported previously, suggests that this animal captures key aspects of the developmental phenotype of human DEE.

Severe anomalies in the brains of *Kcnb1*$^{R312H(+/+)}$ mice

Even simple behavioral responses such as the startle reflex, involve crosstalk between many brain structures including the hippocampus, the amygdala, and the anterior cingulate cortex[21,22]. This suggests that the broad behavioral impairment of the *Kcnb1*$^{R312H(+/+)}$ mouse may underscore diffuse brain anomalies. Indeed the glutamatergic excitatory neurons destined for the UL, do not migrate properly in *Kcnb1*$^{R312H(+/+)}$ embryos, causing anatomical anomalies in the adult brain[2]. Thus, to characterize the impact of the *Kcnb1*^{R312H} allele on neuroanatomy, also in light of the cognitive deficit of the mice, we performed immunofluorescence (IF) in brain slices. The overall thickness of the neocortex, co-immunostained with antibodies that recognize neurofilament medium (NFM) and L1CAM protein is similar in WT and *Kcnb1*$^{R312H(+/+)}$ mice (Fig. 3A, B). However, the relative thicknesses of individual upper layers are altered in the *Kcnb1*$^{R312H(+/+)}$ neocortex, with layer I thicker and layers II and III thinner compared to WT, consistent with the migratory defects of the glutamatergic neurons of those animals[2] (Fig. 3C, D). In contrast, the thickness of individual lower layers (LL) is similar (Fig. 3E, F). These results are summarized in parts of the whole representations in Fig. 3G. Notably, analysis reveals marked histologic alterations in other brain structures including the CC (Fig. 3A, H. Of note, human *KCNB1* DEE-susceptibility alleles are associated with CC anomalies[8]), the bundle of interhemispheric fibers between the CC and the cingulum bundle (Fig. 3I), the cingulum bundle (Fig. 3A, J), the fimbria-fornix (which is implicated in path finding[23], Fig. 3A, K) and the habenular nuclei (Fig. 3A, L). Neuronal histology of the hippocampus, is similar in WT and *Kcnb1*$^{R312H(+/+)}$ slices, in agreement with a previous study that utilized *Kcnb1* Knock Out mice (CA3, Fig. 3A, M)[24].

Electrophysiological attributes are similar in WT and *Kcnb1*$^{R312H(+/+)}$ neurons

Imbalances between excitatory and inhibitory conductances in the brain are a common cause of seizures[25]. Accordingly, a well-established mechanism by which Kv channels cause epilepsy is by dysregulating potassium efflux and consequently, neuronal repolarization[26]. In heterologous expression systems, the amplitude of R312H KCNB1 macroscopic current is greatly decreased compared to WT due to a ~40 mV positive shift in the voltage-dependence[27]. Hence, we hypothesized that the cause of the frequent seizures of the *Kcnb1*$^{R312H(+/+)}$ mice was decreased K^+ current. To test this, we carried out electrophysiological recordings in primary cortical neurons at days in vitro 14 (DIV14). Pyramidal neurons were identified by eye and their identity was confirmed post-electrophysiological recording by amplification of *VGluT1* mRNA a marker of those cells, along with *Kcnb1* mRNA using the polymerase chain reaction analysis of gene expression in single neurons technique of the patch clamp[28] (Fig. 4A, B). Roughly 75% of the cells were positive for *Kcnb1* and *VGluT1* and those neurons were used in the analysis. Representative families of whole-cell K^+ currents (I_K) elicited in WT and *Kcnb1*$^{R312H(+/+)}$ neurons are illustrated in Fig. 4C. Macroscopic current-voltage relationships (I–V), and normalized macroscopic conductance (G/G_{Max}, Eq. 1) are plotted in Fig. 4D, E. Interestingly, no differences are apparent between the properties of WT and *Kcnb1*^{R312H} macroscopic current. We estimated the single-channel current (i) and open probability (p_o) using noise-variance analysis[29]. Whole-cell currents were evoked by 10–20

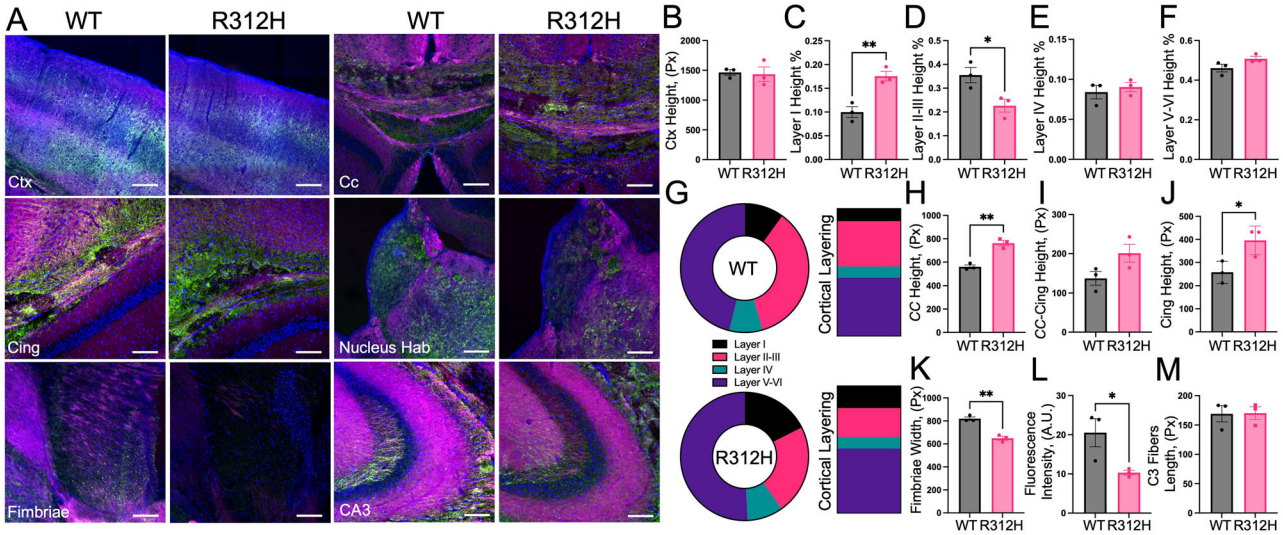

Fig. 3 | The brain of *Kcnb1*$^{R312H(+/+)}$ mice shows diffuse neuronal damage. **A** Representative confocal visualizations of neocortical neurons co-immunostained with NFM (green) and L1CAM (magenta) in the indicated areas of the brain (cortex CTX, corpus callosum CC, cingulum Cing, nucleus habenular nucleus hab, fimbria Fimbriae, CA3 region of the hippocampus: CA3) in WT and *Kcnb1*$^{R312H(+/+)}$ brain slices. DAPI (blue color). Scale bars CTX: 200 µm. Others: 100 µm. **B**–**F** Quantifications of the mean neocortex thickness (**B**) and of individual layers (from left to right, **C** layer I, **D** layers II–III, **E** layer IV, and **F** layers V–VI) in WT and *Kcnb1*$^{R312H(+/+)}$ (R312H) slices. **G** Part of the whole representations of the thickness of the cortical layers in WT and *Kcnb1*$^{R312H(+/+)}$ brain slices. **H** Quantifications of the mean CC bundle of WT and *Kcnb1*$^{R312H(+/+)}$. **I** As in (**H**) for the mean cingulum-CC bundle. **J** As in (**H**) for the mean cingulum bundle height. **K** As in (**H**) for the mean fimbria width. **L** As in (**H**) for the habenular nuclei. **M** As in (**H**) for the fibers of the CA3 region of the hippocampus. Slices were cut from three-month-old brains/genotypes at Bregma coordinates −1.46 mm/−1.58 mm (mouse brain atlas[82]). $^{*}P < 0.05$ and $^{**}P < 0.01$, two-tailed student *t*-test.

consecutive voltage jumps from a holding voltage of −80 mV to 40 mV. Mean current, *I*, and mean-variance σ^2, were calculated and fitted to Eq. 5 (Fig. 4F). Likewise for the macroscopic features of the current, we did not detect differences in the estimated single-channel current and open probability (Eq. 6) of WT and R312H Kcnb1 channels. Together these findings prompt two possible scenarios: either the R312H mutant conducts normally in primary pyramidal neurons or vice versa, the WT channel is electrically silent in those cells. To distinguish these two possibilities we isolated Kcnb1 current (I_{Kcnb1}) from I_K, using 100 nM Guangxitoxin 1-E (GxTx) in the bath[27,30,31]. The toxin similarly blocked I_{Kcnb1} in WT and *Kcnb1*$^{R312H(+/+)}$ neurons, providing the first indication that R312H Kcnb1 mutant channels conduct normally in primary neurons (Fig. 4G, H). However, GxTx blocks Kcnb1 and Kcnb2 channels with equal potency[31]. Even though Kcnb2 is expressed only in layers II and V, to rule out potential effects due to blockage of Kcnb2 channels, we recorded in neurons lacking Kcnb1 channels, obtained from *Kcnb1*$^{NULL(+/+)}$ embryos[32]. The *Kcnb1*$^{NULL(+/+)}$ mouse bears a mutated allele that contains a stop sequence in the voltage-sensor domain, giving rise to a truncated Kcnb1 protein that is degraded and does not reach the plasma membrane[2]. Thus, macroscopic NULL current amplitudes at +80 mV in the absence/presence of GxTx are illustrated in Fig. 4H, and a family of currents, along with I–V and G/G_{Max} relationships are illustrated in Fig. S1A–D. As expected, macroscopic K^+ currents in *Kcnb1*$^{NULL(+/+)}$ neurons are significantly smaller than WT currents and are insensitive to GxTx. In fact, the magnitude of NULL currents is comparable to that of WT (or R312H) currents in the presence of GxTx, indicating that the toxin primarily blocks Kcnb1 channels. We also observe a ~15 mV rightward shift in the voltage dependence of NULL currents, further suggesting that Kcnb1 conducts an important voltage-dependent K^+ current in primary cortical neurons. We next carried out whole-cell current clamp experiments to characterize the excitability of WT and *Kcnb1*$^{R312H(+/+)}$ neurons. We assessed the passive membrane properties of the cells under resting conditions and did not find significant differences in the rheobase, input resistance, cell capacitance, and resting membrane potential of WT and *Kcnb1*$^{R312H(+/+)}$ neurons (Fig. 5A–D). The spikes fired by the neurons of the two genotypes have similar amplitudes, half width (Fig. 5E, 5F), rise time (WT = 0.77 ± 0.05 ms; *Kcnb1*$^{R312H(+/+)}$ = 0.68 ± 0.018 ms, nss, $N = 18$ neurons/genotype, two-tailed *t*-test) and decay time (WT = 1.17 ± 0.06 ms; *Kcnb1*$^{R312H(+/+)}$ = 1.32 ± 0.07 ms, nss, $N = 18$ neurons/genotype, two-tailed *t*-test). Overall, the electrophysiological characteristics of WT and *Kcnb1*$^{R312H(+/+)}$ pyramidal neurons in culture appear to recapitulate those of native cells[33]. Most importantly, WT and *Kcnb1*$^{R312H(+/+)}$ cells fire at similar repetitive spike frequencies, which saturate in the same range of input currents and increase by ~50% in the presence of GxTx (Fig. 5H–5I). *Kcnb1*$^{NULL(+/+)}$ neurons fire at frequencies comparable to those of WT (or *Kcnb1*$^{R312H(+/+)}$) cells in the presence of GxTx but are insensitive to the toxin (Figs. 5I and S1E, F). Furthermore, the passive characteristics of the *Kcnb1*$^{NULL(+/+)}$ membranes are similar to those of WT (or *Kcnb1*$^{R312H(+/+)}$) membranes (Fig. S1G–J). Overall, these data led us to conclude that the ionic properties of R312H Kcnb1 mutant channels in cultured primary pyramidal neurons are normal.

Vesicular glutamate transport is dysregulated in DEE mice

Since electrophysiological analysis rules out an ionic cause for the severe seizure phenotype of the *Kcnb1*$^{R312H(+/+)}$ mouse, we sought to identify alternative, non-ionic, mechanisms. IKCs are expressed in glutamatergic excitatory neurons, and dysregulated glutamate release is causative of seizures. Thus, we determined the levels of vesicular glutamate transporter (VGluT) isoforms 1 and 2 by western blot/densitometry (WBD, Fig. S2) and immunofluorescence (Figs. 6 and S3)[34]. WBD analysis reveals significant upregulation of VGluT1 and VGluT2 protein in *Kcnb1*$^{R312H(+/+)}$ brains compared to WT. The levels of control proteins, glutamic acid decarboxylase, isoform 65 (GAD65), which along with GAD67, provide the major supply of inhibitory gamma-aminobutyric acid (GABA) in the brain, and of synaptosomal-associated protein, 25 kDa (SNAP-25), a key component of the *trans*-SNARE complex are similar in the two genotypes[35,36]. The expression of the two VGluT isoforms is mostly complementary[37,38]. VGluT1 is mainly expressed in excitatory neurons of the neocortex, hippocampus, and cerebellum. VGluT2 is expressed in layer IV of the neocortex, thalamus, and hypothalamus. Immunofluorescence reveals marked differences in VGluT expression between WT and *Kcnb1*$^{R312H(+/+)}$ (Fig. 6A, C). Immunoreactivity to VGluT1 is mostly decreased whereas that to VGluT2 is mostly increased across the various sub-anatomical parts of

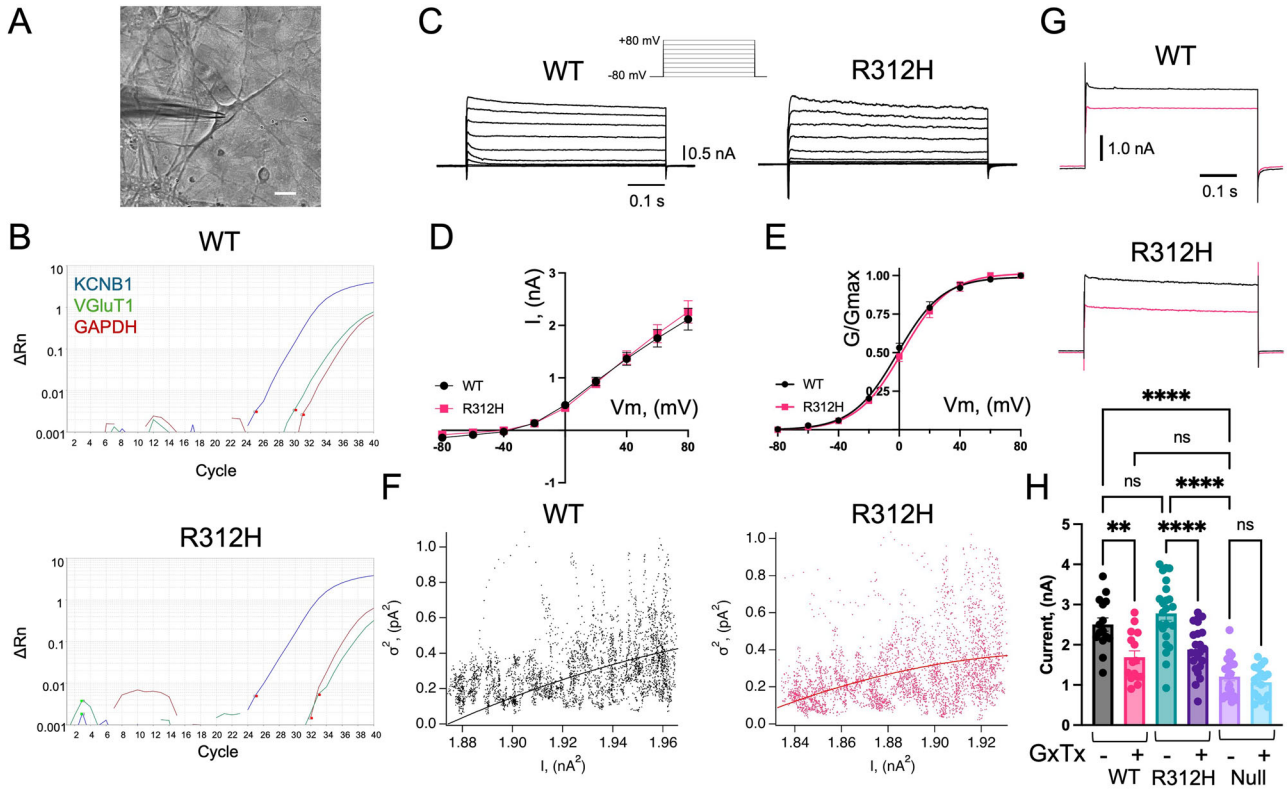

Fig. 4 | K^+ currents are similar in WT and *Kcnb1*$^{R312H(+/+)}$ primary neurons. **A**, **B** Representative image of a typical cortical pyramidal neuron patched to a glass pipette and RT-PCR amplification of *Kcnb1*, *VGluT1*, and for control, Glyceraldehyde 3-phosphate dehydrogenase (*GAPDH*), mRNA transcripts. RT-PCR was carried out using the cell's cytoplasm collected at the end of the electrophysiological recording as described. Scale bar 20 µm. **C** Representative whole-cell currents elicited in a WT or *Kcnb1*$^{R312H(+/+)}$ pyramidal neuron. Cells were clamped at −80 mV and currents were evoked by 0.5 s voltage steps from −80 mV to +80 mV in 20 mV increments (*inset*). **D** Mean macroscopic current-voltage relationships for WT and *Kcnb1*$^{R312H(+/+)}$. $N = 40$ cells/genotype. **E** Macroscopic normalized conductances (G/G_{Max}) for WT and *Kcnb1*$^{R312H(+/+)}$. G/G_{Max} were calculated according to Eq. 1, averaged, and fitted to the Boltzmann function (Eq. 2) with $V_{1/2} = -1.18$ mV and $V_s = 14.9$ mV for WT and $V_{1/2} = 2.09$ mV and $V_s = 15.2$ mV for *Kcnb1*$^{R312H(+/+)}$. $N = 40$ cells/genotype. **F** Representative variance-mean current plots for WT and *Kcnb1*$^{R312H(+/+)}$. Currents were evoked by 10–20, repetitive voltage jumps from −80 mV to +40 mV. Data were fitted to Eq. 5 with $i = 6.3$ pA, $N_c = 558$ channels for WT and $i = 5.1$ pA, and $N_c = 543$ channels for *Kcnb1*$^{R312H(+/+)}$. The estimated p_0 at +40 mV (Eq. 6), is ~0.5 for both genotypes. **G** Representative WT and *Kcnb1*$^{R312H(+/+)}$ currents at +80 mV in the absence/presence of 100 nM Guangxitoxin (GxTx) in the bath. **H** Quantifications of WT, *Kcnb1*$^{R312H(+/+)}$, and *Kcnb1*$^{NULL(+/+)}$ current amplitudes at +80 mV in the absence/presence of 100 nM GxTx in the bath. All recordings were performed using DIV14 neurons, obtained from $N = 7$ WT brains, $N = 7$ *Kcnb1*$^{R312H(+/+)}$ brains, and $N = 5$ *Kcnb1*$^{NULL(+/+)}$ brains with three dishes/brain. $^{*}P < 0.05$, $^{***}P < 0.001$, and $^{****}P < 0.0001$, one-way ANOVA with Tukey's post hoc test.

the cortex, from the retrosplenial granular to the perirhinal region, in *Kcnb1*$^{R312H(+/+)}$ compared to WT (Figs. 6B, C and S2, S3). In addition, VGluT1 and VGluT2 immunoreactivity is significantly dysregulated in other brain structures, notably the amygdala, thalamus, and hypothalamus (Fig. 6A, C). We conclude that the *Kcnb1*$^{R312H(+/+)}$ brain is affected by extensive dysregulation of glutamatergic vesicular transmission.

Neuronal connectivity is disrupted in Kcnb1$^{R312H(+/+)}$ brains

The anatomical anomalies of *Kcnb1*$^{R312H(+/+)}$ brains, along with the morphological defects of their neurons previously observed, and their dysregulated glutamatergic release are likely to have an impact on the connectivity of those cells, as excitotoxicity is a well-established cause of axonal damage[39]. The neocortical pyramidal neurons that express the IKC are divided into three classes: intratelencephalic that project in the neocortex and striatum, pyramidal tract that project into the striatum, and corticothalamic that project into the thalamus[40]. We visualized corticothalamic and corticocortical projections with antegrade biotinylated dextran BDA 488 MW3000 dye injected into the neocortex (Fig. 7), and independently, with retrograde Fluorogold dye injected into the thalamus (Fig. S4), and thalamocortical projections with the antegrade BDA 594 MW3000 dye injected into the thalamus (Fig. S5). Representative z-stack images of antegrade BDA 488 MW3000 visualizations of axonal projections and thalamic neuronal bodies are illustrated in Fig. 7A, B. Examination of z-stack magnifications reveals markedly fewer fibers in the corpus callosum (CC), in the subcortical layer where the efferent fibers divide to project either in the thalamus or in the contralateral cortex (IPS CX to CC), in the contralateral cortex (CNT CX), in the internal capsule (Cp) and in the thalamus (Tha) of the *Kcnb1*$^{R312H(+/+)}$ brain compared to WT (Fig. 7B). Experiments with Fluorogold and BDA 594 MW3000 further reveal significant impairment of corticothalamic and thalamocortical projections in the *Kcnb1*$^{R312H(+/+)}$ brain (Fig. S4 and S5). To better visualize connectivity, we constructed heat maps of BDA 488 MW3000 anterograde tracing (Fig. 7C and Video S1). The maps reveal broad alterations in the connectivity of the *Kcnb1*$^{R312H(+/+)}$ brain, which are particularly appreciable in the cortical and thalamic areas. Of note, corticothalamic projections are virtually absent in the M1 and S1 cortical structures and the CC of the *Kcnb1*$^{R312H(+/+)}$ brain. Likewise, thalamic VPM and VPL areas in the *Kcnb1*$^{R312H(+/+)}$ brain also have lesser projections than the WT brain. Summary quantifications are illustrated in Fig. 7D. The number of contralateral (CNT) and CC fiber and thalamic (Tha) neurons positive to the dyes are significantly decreased in *Kcnb1*$^{R312H(+/+)}$ compared to WT, confirming the existence of extensive connectivity disruption. In contrast, ipsilateral (IPS) connections do not significantly differ between the two genotypes, as expected.

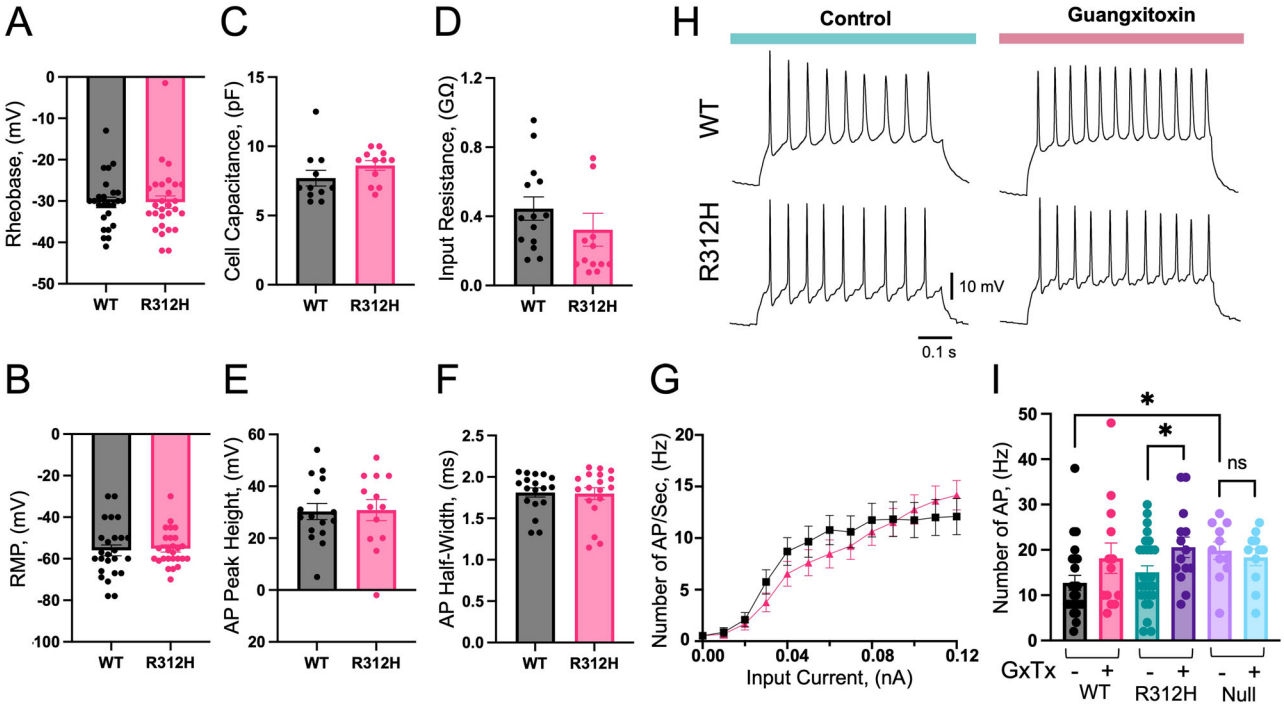

Fig. 5 | Similar firing patterns in WT and *Kcnb1*$^{R312H(+/+)}$ primary neurons. **A**–**D** Passive membrane properties of WT and *Kcnb1*$^{R312H(+/+)}$ primary neurons: **A** rheobase; **B** resting membrane potential (RMP), **C** capacitance, and **D** input resistance. **E** Mean height of the action potential (AP) fired by WT or *Kcnb1*$^{R312H(+/+)}$ neurons. **F** Mean half width of the AP fired by WT or *Kcnb1*$^{R312H(+/+)}$ neurons. **G** Spike frequency as a function of input current for WT and *Kcnb1*$^{R312H(+/+)}$ neurons. $N = 26$ cells/genotype. **H** Representative current-clamp recordings of the electrical activity of a WT and a *Kcnb1*$^{R312H(+/+)}$ primary neuron in the absence/presence of 100 nM GxTx. Firing activity was triggered by a 100 pA current injection. **I** Spike frequency induced by 50 pA current injection in WT, *Kcnb1*$^{R312H(+/+)}$, and *Kcnb1*$^{NULL(+/+)}$ neurons in the absence/presence of 100 nM GxTx in the bath. All recordings were performed using DIV14 neurons, obtained from $N = 7$ WT brains, $N = 7$ *Kcnb1*$^{R312H(+/+)}$ brains, and $N = 5$ *Kcnb1*$^{NULL(+/+)}$ brains with three dishes/brain. $^{*}P < 0.05$, two-tailed student's *t*-test.

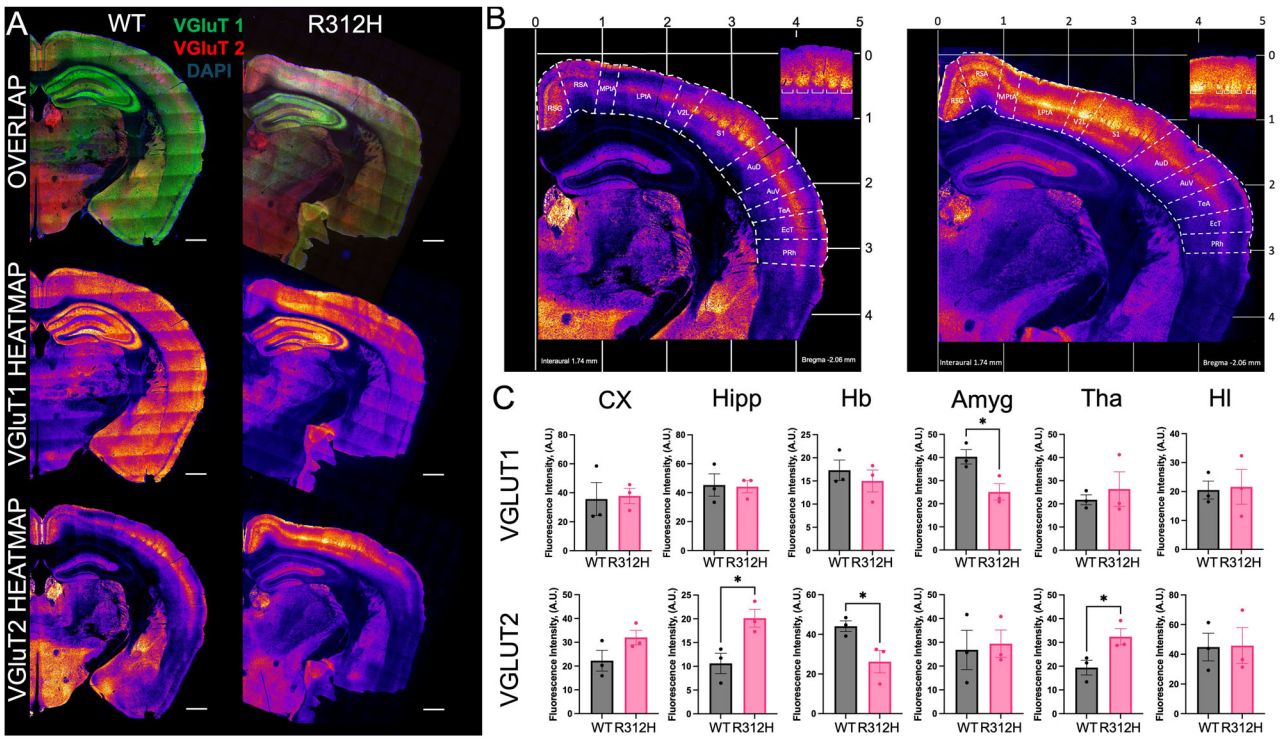

Fig. 6 | Dysregulated glutamatergic vesicular transport in the *Kcnb1*$^{R312H(+/+)}$ brain. **A** Representative confocal tile images of WT and *Kcnb1*$^{R312H(+/+)}$ coronal brain sections showing overlap of VGluT1, VGluT2 and DAPI and heat maps of VGlut1 or VGluT2 fluorescence (blue is the lowest fluorescence). Scale bars 200 µm. **B** Magnifications of the heat maps of immunostainings in (**A**) showing VGluT2 expression in the various cortical parts. Insets: magnifications of the barrel cortex (S1). **C** Quantifications of VGluT1 and VGluT2 immunostaining in the various areas of the brain. CX cortex, Hipp hippocampus, Hb habenular nuclei, Amyg amygdala, Tha thalamus, Hl hypothalamus. $N = 3$ three months old brains/genotype. $^{*}P < 0.05$, two-tailed student's *t*-test.

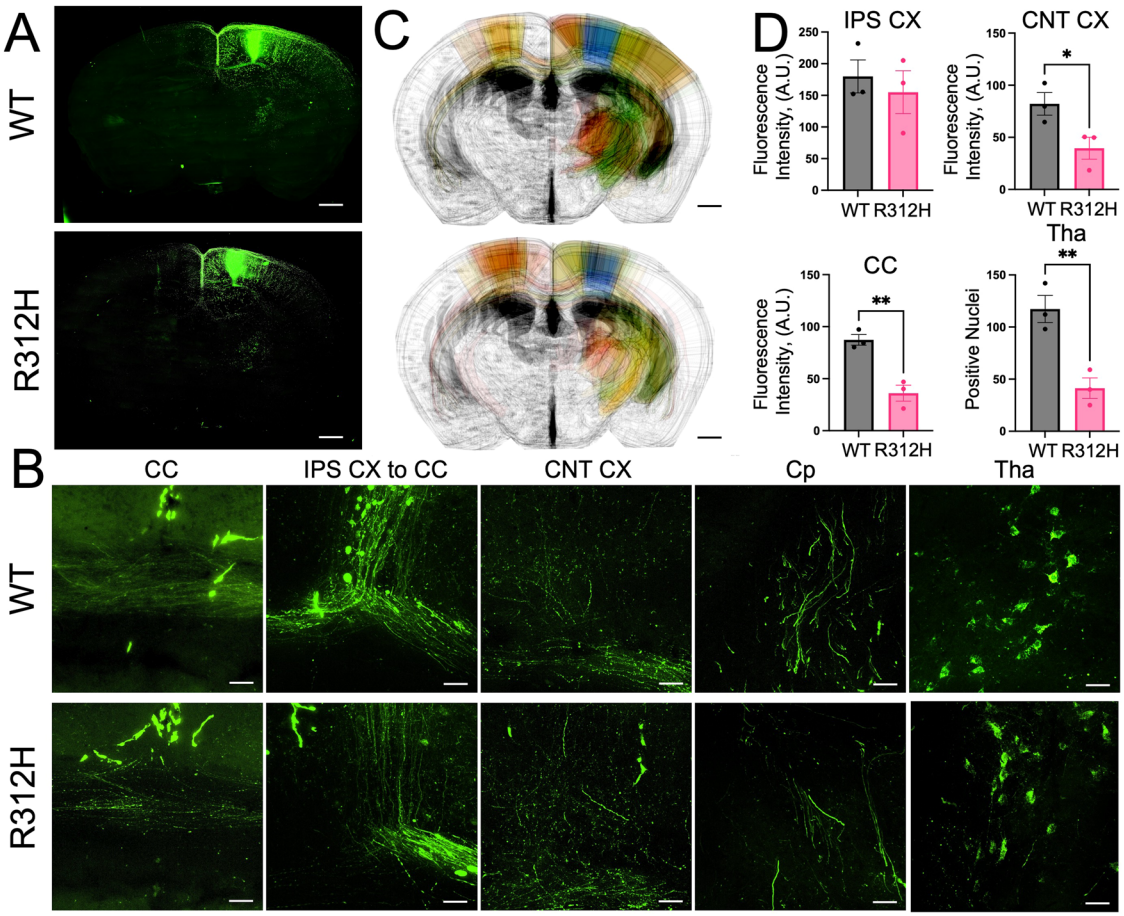

Fig. 7 | Disrupted neuronal connectivity in *Kcnb1*$^{R312H(+/+)}$ mice. A Representative z-stack reconstructions ($N = 20$ sections) of corticocortical and corticothalamic connections in a WT and *Kcnb1*$^{R312H(+/+)}$ brain visualized with antegrade BDA 488 MW3000 injected into the neocortex. Scale bars 200 µm. **B** Representative z-stack magnifications of the images in (**A**) visualizing the indicated brain structures (CC corpus callosum; IPS CX to CC efferent ipsilateral cortical fibers in the CC, CNT CX contralateral cortex—specular to the site of injection of the tracer, Cp internal capsule, Tha thalamus). Scale bars 50 µm. **C** Connectivity z-stack (30 images) maps for WT and *Kcnb1*$^{R312H(+/+)}$ were drawn from experiments with BDA 488 MW3000. Colors illustrate the density of projections (in %) ranging from green (66–100%) to bronze (33–65%) to red (0–32%). The blue color is the site of the injection. $N = 4$ brains/genotype. Scale bars 0.2 cm. **D** Quantifications of connectivity assessed with BDA 488 MW3000 in the ipsilateral cortex (IPS CX), contralateral cortex (CNT CX), Thalamus (Tha), and CC in WT and *Kcnb1*$^{R312H(+/+)}$ mice. BDA MW3000 Alexa 488, was injected into the cortex at the following coordinates in mm: Mid: − 1.2, Bregma: −0.6, Top: −1.0. Images were taken from three-month-old brain slices cut at the following coordinates in mm: CC Mid = 0; Bregma = −0.6, Top = −1.2. IPS CX to CC Mid = −1.2; Bregma = −0.6 and Top = −1.0. CNT CX: Mid = 1.2, Bregma = −0.6 and Top = −1.0. Cp: Mid = −2.0, Bregma = −1.06/−1.22 and Top = −2.5/-3.0. Tha: Mid = −1.8, Bregma = −1.34/−1.46 and Top = −3.0. $^{*}P < 0.05$ and $^{**}P < 0.01$, two-tailed student's *t*-test.

Axonal damage is extensive in *Kcnb1*$^{R312H(+/+)}$ brains

To further elucidate how defects in connectivity affect the *Kcnb1*$^{R312H(+/+)}$ brain, we used immunofluorescence to assess potential axonal destruction. We focused the analysis on the CC as this structure has a high content of white matter and its agenesis is associated with seizures, intellectual disability, and motor impairment[41]. Thus, eye inspection of z-stack reconstructions of corpi callosi immunostained with SMI32 antibody that recognizes hypophosphorylated heavy chain neurofilament (NFH, Fig. S6A), and quantitative analysis (Fig. S6B), uncovers a significant accumulation of NFH in *Kcnb1*$^{R312H(+/+)}$ compared to WT, a typical feature of axonal vulnerability[42]. Another marker, histone deacetylase 1 (HDAC1), which is translocated from the nucleus into degenerating axons, underscores extensive injury in the *Kcnb1*$^{R312H(+/+)}$ fibers (Fig. S6A)[43]. The percentage of translocated HDAC1 over the total nuclear protein changed from a physiological 8% in WT to a significant 24% in *Kcnb1*$^{R312H(+/+)}$, a 300% increase (Fig. S6C. Manders's coefficients for HDAC1-DAPI co-localization, M1 = 0.71 and M2 = 0.78 for WT and M1 = 1.0 and M2 = 0.99 for *Kcnb1*$^{R312H(+/+)}$[44]). To assess the condition of the axon initial segment and of the Nodes of Ranvier we stained the slices with an antibody against neuronal Ankyrin-G. Representative images, along with quantifications are shown in Fig. S7. Immunofluorescence to Ankyrin-G is more than halved in the *Kcnb1*$^{R312H(+/+)}$ neocortex compared to WT, disclosing broad axonal damage in the former. In contrast, the Ankyrin-G signal is similar in the hippocampi of WT and *Kcnb1*$^{R312H(+/+)}$ corroborating previous observations (Fig. 3) that indicate that the *Kcnb1*^{R312H} mutation only marginally affects the hippocampus. In summary, these data pinpoint at least two potentially ictogenic mechanisms in the *Kcnb1*$^{R312H(+/+)}$ brain: diffuse axonal destruction and corresponding connectivity and dysregulated glutamatergic transmission. These alterations are likely to produce hyperexcitability and uncoordinated firing, which are well-established seizure triggers.

The IKC is implicated in actin dynamics

Many aspects of the *Kcnb1*$^{R312H(+/+)}$ phenotype including defective neuronal migration, aberrant neuronal morphology, and decreased synapse functionality are dependent on the actin cytoskeleton[2,45,46]. As the ability to interact with actin is a major physiological function of integrins, this may imply that the inability to establish proper IKC-actin filament bonds and/or to modulate the formation of new filaments may be causative of the morphological and synaptic anomalies in the *Kcnb1*$^{R312H(+/+)}$ mutant[47–52]. In fact, IKC/integrin signaling is impaired in those animals[2]. To determine whether

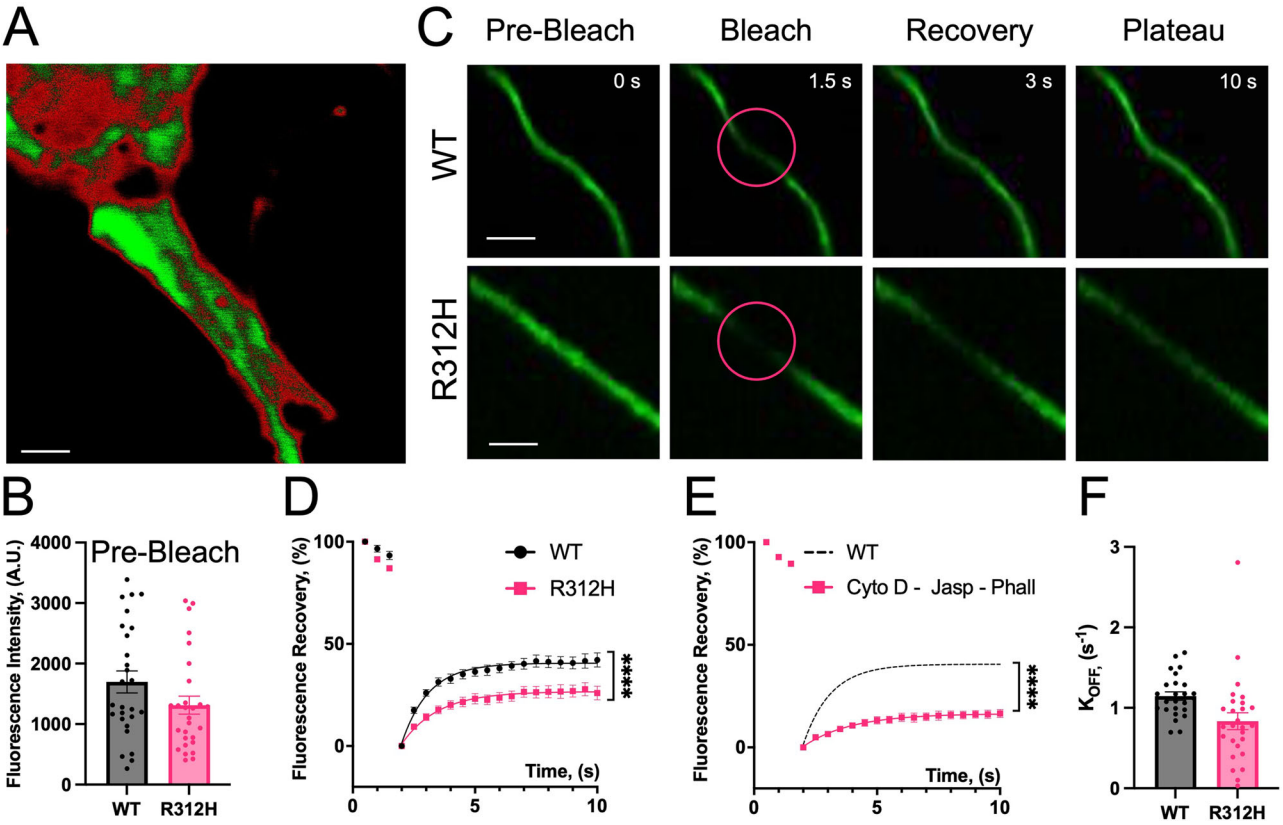

Fig. 8 | Actin polymerization is impaired in *Kcnb1*$^{R312H(+/+)}$ cells following FRAP. **A** Representative confocal visualization of actin (green color) in a WT basal dendrite expressing Lifeact-GFP. Part of the soma is visible in the upper left corner. Scale bars 1 µm. **B** Lifeact-GFP fluorescence at baseline, before photobleaching in WT and *Kcnb1*$^{R312H(+/+)}$ dendrites. **C** Representative confocal images of a WT and *Kcnb1*$^{R312H(+/+)}$ basal dendrite before and after photobleaching. The circle illustrates the area under which GFP intensity was measured. Scale bars 5 µm. **D** Mean FRAP in WT (black circles) or *Kcnb1*$^{R312H(+/+)}$ (magenta squares) dendrites. Fluorescence recovery was calculated according to Eq. 7. Solid lines fit the data to a single exponential function (89). $N = 28–30$ cells/genotype. **E** Mean FRAP in WT in the absence ($N = 28$ cells)/presence ($N = 15$ cells) of 45 nM Cytochalasin D, 15 nM Phalloidin and 30 nM Jasplakinolide. **F** k_{off} rate was obtained by fitting individual FRAP responses to a single exponential function (Eq. 8) for WT and *Kcnb1*$^{R312H(+/+)}$. All measurements were taken using DIV14 neurons. $^{*}P < 0.05$ and $^{****}P < 0.0001$, one-way ANOVA with Tukey's post hoc test.

the IKC is part of the actin machinery, we performed Fluorescence Recovery after Photobleaching (FRAP) in WT and *Kcnb1*$^{R312H(+/+)}$ cortical neurons[53]. Neurons were transfected with Lifeact-GFP, which allows visualization of filamentous actin (F-actin)[54]. A representative confocal image visualizing actin in a WT basal dendrite is illustrated in Fig. 8A. Lifeact-GFP fluorescence was determined before photobleaching to detect differences due to transfection efficiency and in case, normalize data to baseline response. However, fluorescence levels were similar prior to photobleaching in all conditions, indicating that transfection efficiency was stable and genotype-independent (Fig. 8B). Thus, following photobleaching of pyramidal neurons basal dendrites, GFP fluorescence in WT and *Kcnb1*$^{R312H(+/+)}$ cells partially recover in a time-dependent manner, with a mobile fraction that accounts for ~40% and ~20%, respectively (Fig. 8C, D). To account for possible diffusion of unbound Lifeact into the photobleached area, we carried out FRAP in the presence of a mixture of cytoskeletal toxins, namely Cytochalasin D (CytoD), Phalloidin (Phall) and Jasplakinolide (Jasp). The rationale is that by freezing the polymerization of actin, any residual GFP fluorescence in the photobleached area should reflect unbound Lifeact. However, fluorescence recovery was significantly impaired in the presence of the mixture of cytoskeletal toxins indicating that the diffusion of unbound Lifeact is negligible in our FRAP assays (Fig. 8E). The time course of fluorescence recovery, $R(t)$, is dependent upon many factors including the diffusion and the binding/unbinding of Lifeact-GFP to F-actin and a detailed characterization of the dynamics of these processes was beyond the scope of this study[53]. We assumed that the diffusion of Lifeact-GFP is dominant over its rate of association or dissociation from F-actin (reaction-limited process). Under these conditions, $R(t)$ recovers exponentially with a time constant given by the inverse of the dissociation rate (Eq. 8). Accordingly, WT and *Kcnb1*$^{R312H(+/+)}$ fluorescence recovery is well fit to a single exponential function, with comparable k_{off} rates ($k_{off} \sim 1.1\ s^{-1}$ and $k_{off} \sim 0.8\ s^{-1}$, respectively, Fig. 8F). This suggests that Lifeact-GFP binds to F-actin similarly in the two genotypes, and therefore that the FRAP signal reflects actin remodeling events.

Integrins and Kcnb1 channels differentially affect FRAP in WT and Kcnb1$^{R312H)+/+)}$ neurons

If the IKC is implicated in actin dynamics, manipulations that activate the integrins and/or the Kcnb1 channel should affect fluorescence recovery. To begin to test this hypothesis, we performed FRAP in the presence of Fibronectin (FN) an activator of RGD integrins, such as integrin-α5[55]. The treatment improved fluorescence recovery in WT and *Kcnb1*$^{R312H(+/+)}$ neurons (Fig. 9A, B, F, G). However, fibronectin is roughly twice as much as potent in *Kcnb1*$^{R312H(+/+)}$ than in WT neurons. Moreover, if Kcnb1 interacts with the integrins of the IKC, blocking the channel with GxTx should affect the fibronectin response. Indeed, the effect of fibronectin on the FRAP of WT is almost suppressed (Fig. 9A, F). In contrast, GxTx does not appreciably alter the fibronectin response of *Kcnb1*$^{R312(+/+)}$ cells (Fig. 9B, G). We next sought to determine the effect of activating the Kcnb1 channel by raising $[K]_o$, to induce cell depolarization, as done before[27]. The results of those experiments, summarized in Fig. 9C, D, and Fig. 9F, G indicate that high $[K]_o$ enhanced the FRAP in both WT and *Kcnb1*$^{R312H(+/+)}$ neurons. Like with fibronectin, the enhancement of fluorescence recovery is relatively

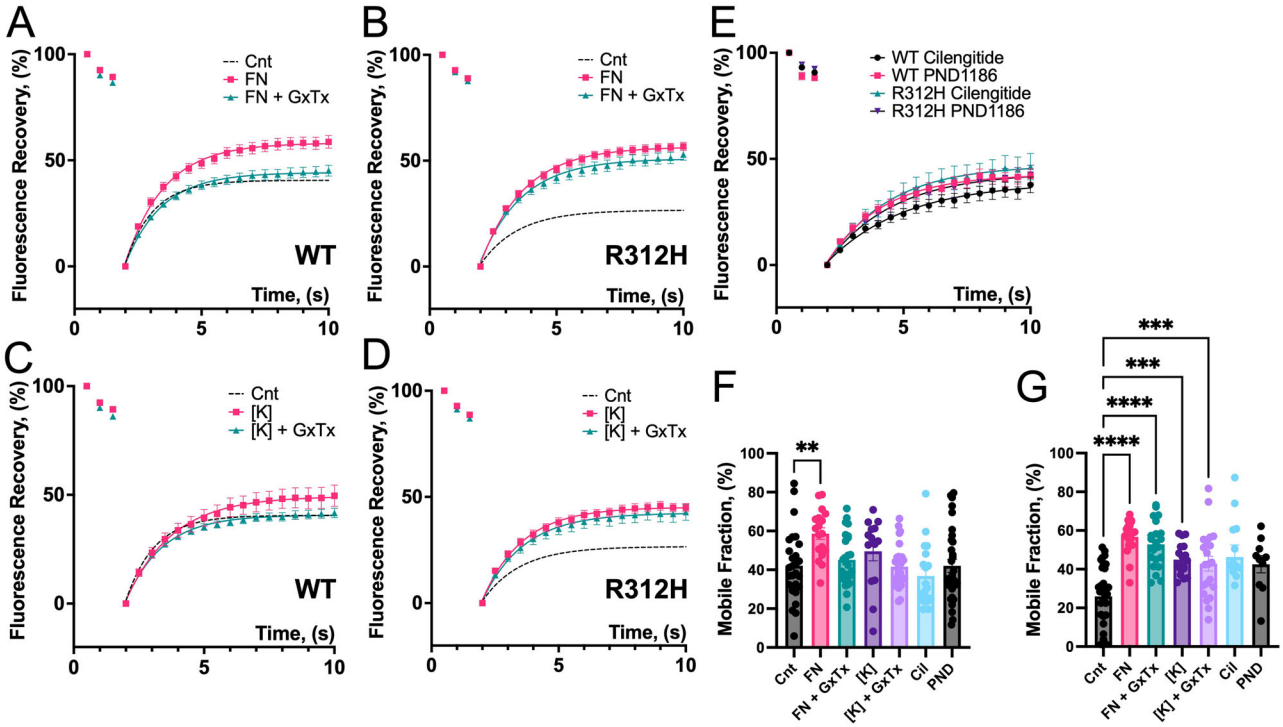

Fig. 9 | The IKC modulates actin polymerization through integrins. A FRAP in WT dendrites in the absence (Cnt, dotted line, $N = 28$ cells) or presence of 50 µg/mL fibronectin (FN, squares, $N = 18$ cells) or 50 µg/mL FN + 100 nM GxTx (FN + GxTX, triangles, $N = 26$ cells) applied 15 min before FRAP. **B** As in (**A**) for $Kcnb1^{R312H(+/+)}$ dendrites. $N_{Cnt} = 30$ cells; $N_{FN} = 20$ cells; and $N_{FN+GxTx} = 21$ cells. **C** FRAP in WT dendrites in the absence (Cnt. dotted line, $N = 28$ cells) or presence of 30 mM $[K]_o$ ($[K]$, squares, $N = 14$ cells) or 30 mM $[K]_o$ + 100 nM GxTx ($[K]$ + GxTx, triangles, $N = 27$) applied 5 min before FRAP. **D** As in (**C**) for $Kcnb1^{R312H(+/+)}$ neurons. $N_{Cnt} = 30$ cells; $N_{K+} = 18$ cells and $N_{K+GxTx} = 22$ cells. **E** FRAP in WT and $Kcnb1^{R312H(+/+)}$ dendrites in the presence of 100 nM Cilengitide (Cil, WT circles, $N = 19$ cells; R312H triangles, $N = 13$) or 10 nM PND-1186 (PND, WT squares, $N = 22$; R312H triangles, $N = 10$) applied 15 min before FRAP. **F** Mobile fraction (fluorescence recovery at time =10 s) for WT neurons subjected to the indicated experimental conditions. **G** Mobile fraction for $Kcnb1^{R312H(+/+)}$ neurons subjected to the indicated experimental conditions. All measurements were taken on DIV14 neurons. $^{*}P < 0.05$, $^{**}P < 0.01$, $^{***}P < 0.001$, and $^{****}P < 0.0001$ one-way ANOVA with Tukey's post hoc test.

modest in WT neurons and is completely abolished by GxTx, while in $Kcnb1^{R312H(+/+)}$ cells, fluorescence recovery is greater and GxTx-independent. Taken together, these results prompt several considerations. First, they suggest that both the integrins and the Kcnb1 channels are activated in WT IKCs during FRAP. Second, they rule out the involvement of channels other than Kcnb1 in the FRAP response, otherwise GxTx should only partially suppress the effects of high $[K]_o$ in WT neurons. Third, they seem to exclude a role of Kcnb1 current, as while the electrical properties of WT and $Kcnb1^{R312H(+/+)}$ primary neurons are similar, their FRAP response to GxTx is opposite. It is also worth noticing that the site of interaction of GxTx with the Kcnb1 channel is located in the voltage-sensor domain, where the R to H replacement occurs in the mutant[31]. This may suggest that the voltage-sensor has a role in mediating Kcnb1-integrin interactions and consequently, that the histidine replacement uncouples these interactions in IKCs formed with R312H channels. We next determined the effect of blocking the integrins by using Cilengitide and PND-1186, respectively a specific inhibitor of integrin-α5, and of Focal Adhesion kinase (FAK)—a key component of integrin signaling—that had shown efficacy with IKCs in vivo and in vitro[2,56–58]. Both compounds induced similar FRAP responses in WT and $Kcnb1^{R312H(+/+)}$ cells (Fig. 9E–G) and significantly delayed fluorescence recovery (k_{off} eqn .8. WT: cnt = 1.15 ± 0.05 s^{-1}; Cil = 0.42 ± 0.07 s^{-1} $P = 0.005$; PND = 0.51 ± 0.1 s^{-1} $P = 0.027$. $Kcnb1^{R312H}$: cnt = 0.83 ± 0.1 s^{-1}; Cil = 0.49 ± 0.05 s^{-1} $P = 0.046$; PND = 0.46 ± 0.05 s^{-1} $P = 0.04$, two-tailed *t*-test). We conclude that the IKC is a component of the actin machinery.

G-actin is increased in the DEE brain

Biochemical quantification of F-actin and globular (G) actin in the cortices of three-month-old WT and $Kcnb1^{R312H(+/+)}$ mice is shown in Fig. S8. G-actin is significantly increased in $Kcnb1^{R312H(+/+)}$ compared to WT. At equilibrium, the critical concentration of G-actin, C_c, is given by the ratio between the rate of removal from the filament, k_{off}, and the rate of addition of monomers to the filament polymer, k_{on}, that is, $C_c = k_{off}/k_{on}$[59]. Hence, these data indicate that in $Kcnb1^{R312H(+/+)}$ cortices either the addition of actin molecules to the filament is slowed down, in agreement with FRAP data, or alternatively, that the shredding of actin is accelerated.

The IKC regulates the polymerization of new filaments in immortal cells

Since FRAP and biochemical data suggest that the activity of the IKC may be important for the formation of fast-growing filaments, we sought to corroborate this model by employing cytoskeletal toxins. The underlying idea of this approach is that the effect of a toxin should be amplified when the mechanism it impinges on, is already impaired. Thus, in Chinese hamster ovary (CHO) cells expressing WT or R312H KCNB1 subunits, Phalloidin, Cytochalasin D and Jasplakinolide decreased cell proliferation (Fig. S9A). Likewise, in N2a mouse neuroblastoma cells, Cytochalasin D and Jasplakinolide impaired neurite outgrowth (Fig. S9B). In contrast, Latrunculin A (LatA) had only minor effects in both assays (in both CHO and N2a cell assays the toxins were used at concentrations only moderately toxic to mock-transfected cells). The fact that the toxins are generally harmful is largely expected since these are produced by poisonous fungi and sponges. However, the extent of Cytochalasin D and Jasplakinolide toxicity is genotype-dependent. Cytochalasin D has a significantly greater effect on R312H-expressing cells than on WT-expressing cells (50% impairment vs 70% impairment of neurite outgrowth, $P < 0.0001$ two-tailed *t*-test and 45% vs 65% impairment of proliferation, nss two-tailed *t*-

test, for WT and R312H, respectively). Conversely, Jasplakinolide has greater effects in WT-expressing vs R312H-expressing cells (40% vs 65% impairment of neurite outgrowth, $P < 0.003$ two-tailed *t*-test, and 46% vs 64% impairment of proliferation, nss two-tailed *t*-test, for WT and R312H, respectively). This may unveil differences in the way that IKCs formed with WT or R312H subunits handle the remodeling of the actin filaments. Cytochalasin D caps the barbed end of the fast-growing filament, preventing F-actin elongation. This strengthens the idea that the IKC is implicated in the mechanisms underlying the formation of new filaments, consistent with some of the physiological roles of the complex. Jasplakinolide also enhances actin polymerization by increasing the rate of nucleation. However, the decreased toxicity of Jasplakinolide in R312H-expressing cells could be simply due to increased availability of G-actin (Fig. S8). In contrast, the fact that Latrunculin A and Phalloidin effects are genotype-independent, would rule out the involvement of the IKC in the mechanisms underlying filament depolymerization (Latrunculin A) or stability (Phalloidin).

Genotype-dependent effects of the cytoskeletal toxins on neuronal networking

We next applied the cytoskeletal toxins to WT and $Kcnb1^{R312H(+/+)}$ neurons at the same concentrations used in immortal cells. Representative images of neuronal cultures in the absence/presence of Cytochalasin D, Jasplakinolide, Latrunculin A, and Phalloidin are illustrated in Fig. S10A. Eye inspection indicates that the toxins damage the actin cytoskeleton, as reflected by the disruption of dendritic arborization and networking. To quantify this, we performed a Sholl analysis. Figure S10B indicates the density of intersections, defined as the number of Sholl intersections normalized to the number of cells within an area of radius *r*, in the absence or presence of the four cytoskeletal toxins for WT and $Kcnb1^{R312H(+/+)}$ neurons. For clarity, the density of intersections in correspondence of a distance roughly twenty times the size of the soma of a neuron (200 µm) is illustrated in Fig. S10C. Cytochalasin D is more effective in disrupting dendritic arborization in $Kcnb1^{R312H(+/+)}$ than WT ($P < 0.0001$ two-tailed *t*-test), whereas Jasplakinolide is more efficacious in WT compared to $Kcnb1^{R312H(+/+)}$ (nss, two-tailed *t*-test) and the effects of Latrunculin A and Phalloidin are similar. Thus, as in immortal cells, also in primary neurons the effects of some toxins are genotype-dependent.

Genotype-dependent effects of the cytoskeletal toxins on dendritic development

Images of single neurons in the absence/presence of Cytochalasin D are illustrated in Fig. 10A. The dendrites of individual $Kcnb1^{R312H(+/+)}$ neurons are underdeveloped compared to WT. Those dendrites present large actin aggregates, probably reflecting underlying damage (Fig. 10A arrows). These effects appear to be amplified by Cytochalasin D. Thus, the total dendrite length, (TDL, Fig. 10B), a parameter estimated by Sholl analysis, is decreased in $Kcnb1^{R312H(+/+)}$ neurons compared to WT cells at baseline. Dendritic branching is underdeveloped in $Kcnb1^{R312H(+/+)}$ compared to WT, as indicated by the fact that the Sholl Intersection profiles (SIPs) are narrower and smaller (Fig. 10C). As previously seen, the impact of the various toxins on the TDL and the SIP is genotype-dependent: maximal for Cytochalasin D (TDL: $P < 0.0001$, two-tailed *t*-test; SIP $P < 0.0001$ Kolmogorov–Smirnov test) and Jasplakinolide (TDL: $P < 0.0001$, two-tailed *t*-test; SIP $P < 0.0001$ Kolmogorov–Smirnov test) in $Kcnb1^{R312H(+/+)}$ and WT cells, respectively, and similar for Latrunculin A and Phalloidin.

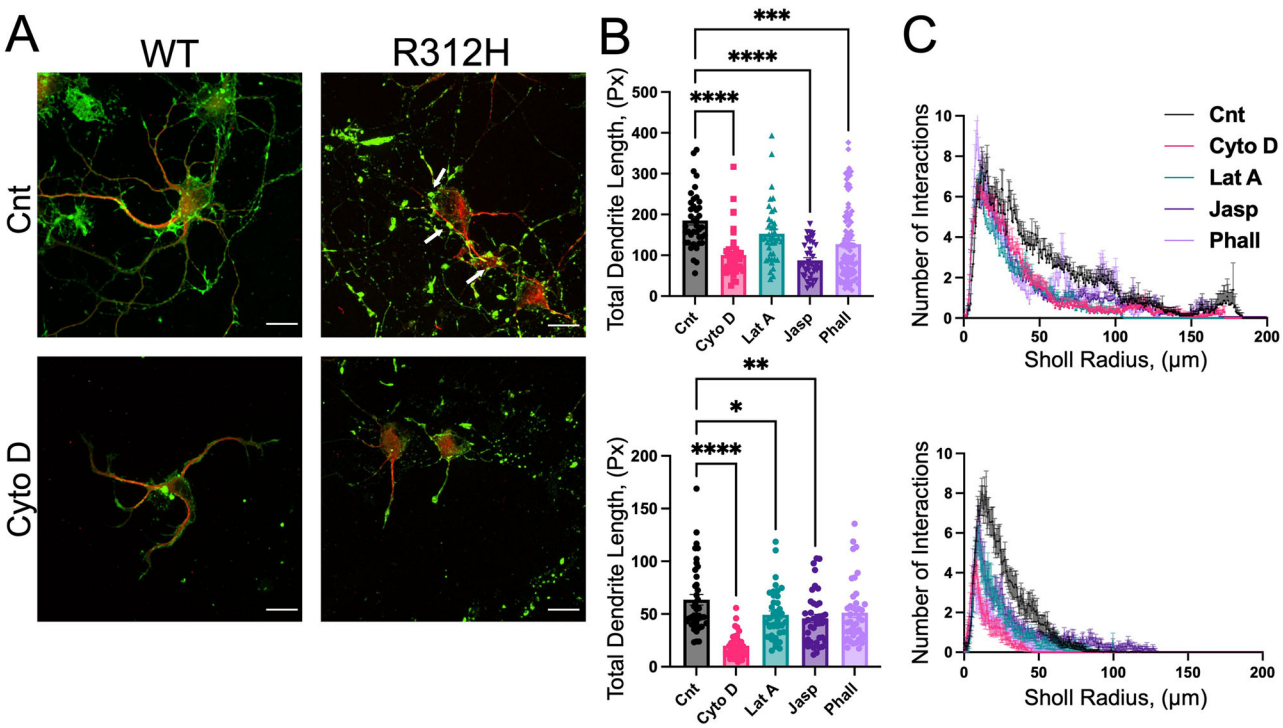

Fig. 10 | Cytoskeletal toxins differentially affect dendritic arborization. **A** Representative confocal images of WT or $Kcnb1^{R312H(+/+)}$ neurons incubated in the absence/presence of 30 nM Cytochalasin D (CytoD). The cells were co-immunostained for actin (green) and Map2 (red) antibodies. Large clumps of actin are demonstrated in $Kcnb1^{R312H}$ cells (arrows). Scale bars 20 µm. **B** Total dendrite length (TDL) estimated by Sholl analysis for WT (upper graph) or $Kcnb1^{R312H(+/+)}$ (lower graph) neurons in the absence/presence of the indicated toxins. **C** Sholl intersection profiles for WT (upper graph) or $Kcnb1^{R312H(+/+)}$ (lower graph) neurons in the absence (black) or presence of the indicated toxins. Within the same genotype, all toxin SIPs are statistically different from the WT SIP ($P < 0.0001$, Kolmogorov–Smirnov test). All measurements were taken using DIV7 neurons. Sholl analysis of individual neurons was performed using Fiji, (ImageJ). In all experiments, toxins were maintained in the media starting at DIV1 at the following concentrations: Cytochalasin D (CytoD, red), 30 nM; Jasplakinolide (Jasp, blue) 30 nM; Latrunculin A (LatA, green), 1 µM and Phalloidin (Phall, light blue), 15 nM. $N = 20$ neurons/genotype/experimental condition from three dams/genotype. $^{*}P < 0.05$, $^{**}P < 0.01$, $^{***}P < 0.001$, and $^{****}P < 0.0001$, one-way ANOVA with Tukey's post hoc test.

Discussion

The goal of this study was to address important questions concerning the molecular basis for IKC function in normal and disease states. We used a mouse model of DEE harboring the *Kcnb1*^{R312H} allele which was originally found in two unrelated DEE children[60]. In addition to severe epilepsy previously reported, homozygote *Kcnb1*^{R312H} mice are affected by extensive neuronal damage in multiple brain areas including the upper layers, fornix, fimbria, habenular nuclei, corpus callosum, and cingulum bundle. The corticothalamic and corticocortical projections of the glutamatergic pyramidal neurons that express the IKC are damaged, along with severe axonal disruption. Most importantly, vesicular glutamatergic transport is grossly dysregulated in the cortex, thalamus, and amygdala. The anomalies of the *Kcnb1*$^{R312H(+/+)}$ brain are associated with robust behavioral deficit, that includes hyperactivity (a common trait of mouse models of DEE and also observed in human patients[14,15,61]), impairment in multiple cognitive domains, and compulsive traits. Notably, while all DEE children are affected by severe developmental and intellectual disability a significant percentage of them present brain anomalies. Overall, the *Kcnb1*$^{R312H(+/+)}$ phenotype appears to recapitulate key aspects of the human DEE pathology.

Loss-of-function (LOF) mutations in Kv channel genes are commonly found in epileptic patients as their products cause an imbalance between excitatory and inhibitory conductances in the brain[25]. The *Kcnb1*^{R312H} allele was considered a LOF as R312H KCNB1 mutant channels expressed in heterologous expression systems conduct poorly due to a ~40 mV rightward shift in the voltage dependence of the channel. As such, R312H KCNB1 mutant channels were expected to make the brain susceptible to seizure onset[26]. Contrary to expectations, the electrical properties of WT and *Kcnb1*$^{R312H(+/+)}$ primary glutamatergic pyramidal neurons turn out to be similar. GxTx similarly blocks WT and *Kcnb1*$^{R312H(+/+)}$ macroscopic K^+ currents and increases spike frequency by roughly ~20% in both genotypes. Thus the fact that R312H Kcnb1 mutant channels conduct normally in primary neurons, seems to rule out the possibility that the epileptic phenotype of the *Kcnb1*^{R312H} mouse is caused by defective conduction of Kcnb1 channels. We also noticed that the impaired connectivity along with dysregulated vesicular glutamatergic transport affecting the *Kcnb1*$^{R312H(+/+)}$ mouse can be causative of seizures, consistent with the fact that in DEE epilepsy is typically drug-resistant[12,13]. Moreover, there is marked neuronal loss in the *Kcnb1*$^{R312H(+/+)}$ brain, which may further constitute a Kcnb1 current-independent ictogenic mechanism[2]. However, additional electrophysiological analyses will be necessary to confirm these results such as for example, recordings in brain slices. Furthermore, compared to heterologous expression systems where R312H KCNB1 channels were expressed alone, native Kcnb1 channels are heteromeric complexes containing electrically silent accessory subunits, including members of the KCNE, KCNF, KCNG, KCNS and KCNV sub-families, most of which affect the voltage-dependence of the complex and thus may compensate for the effects of the R312H mutation[62,63]. Other factors include the lipid composition of the plasma membrane, that modulates the gating of the channel and the developmental stage of the neurons[64]. Nonetheless, if confirmed, the results of this study provide a paradigm shift: first, that normally conducting Kv channels can be ictogenic, and second, that the etiology of DEE is mainly non-ionic. Accordingly, *Kcnb1*$^{R312H(+/+)}$ neurons exhibit marked impairment in the way they handle the formation of new actin filaments. Aberrant actin polymerization is consistent with the dysregulated integrin signaling previously observed in those brains, as the ability to interact with actin is a major component of the adhesive function of integrins[2]. Neuronal actinopathies are relatively infrequent, but actin and its cytoskeleton are emerging as critical players in neurological diseases, including epilepsy[65–68]. As actin plays a crucial role in many fundamental processes including neuronal migration, axon pathfinding, and synaptogenesis, which are all grossly compromised in the *Kcnb1*$^{R312H(+/+)}$ mouse, this may naturally explain the robust phenotype of the mice[45,69–75]. But how do the channels and the integrins interact to modulate the polymerization of actin? Based on the evidence at hand a model that predicts that the structural rearrangements associated with the activity of the channel trigger and control integrin signaling seems the most probable, especially if other, electrically silent subunits are present in the IKC[62,63]. In fact, the observation that R312H channels appear to conduct normally would rule out mechanisms dependent on potassium current but many questions remain unresolved. In addition, it is not known whether the channel provides a substrate for the numerous kinases that are activated by the integrins as Kcnb1's C-terminus is extraordinarily rich in serine/threonine and tyrosine phosphorylation consensus sites[76–78]. Other limitations include the possibility, although unlikely, that the increased G-actin levels in the *Kcnb1*$^{R312H(+/+)}$ cortex might be due to enhanced transcription. All these questions await future investigations.

In summary, this study elucidates the molecular basis of a neurodevelopmental channelopathy that appears to proceed through non-ionic mechanisms. As such, the IKC provides an example of how a single gene can regulate aspects of neuronal function as varied as excitability, development, and morphology.

Methods

Table of reagents

REAGENT or RESOURCE	SOURCE	IDENTIFIER
Antibodies		
Anti-MAP2 antibody	Abcam	Cat# ab5392
Anti-VGluT1 antibody	Thermo Fisher Scientific	Cat# MA531373 RRID:AB_2787010
Anti-VGluT2 antibody	Abcam	Cat# ab216463 RRID:AB_2893024
Anti-GAD65 antibody	Thermo Fisher Scientific	Cat# PA522260 RRID:AB_11154107
Anti-SNAP25 antibody	Thermo Fisher Scientific	Cat# PA1-740 RRID:AB_2192212
Anti-Ankyrin G antibody	Thermo Fisher Scientific	Cat# 33-8800 RRID:AB_2533145
Anti-neural cell adhesion molecule L1 antibody, clone 324	Millipore Sigma	Cat# MAB5272 RRID:AB_2133200
Anti-HDAC-1 antibody	Thermo Fisher Scientific	Cat# PA1-860 RRID:AB_2118091
Anti-SMI32 antibody	BioLegend	Cat#801702 RRID: AB_2715852
Anti-NF-M antibody	Abcam	Cat# ab7794 RRID: AB_306083
Anti-actin antibody, clone C4	Millipore	Cat# MAB1501, RRID:AB_2223041
Anti-potassium channel Kv2.1 antibody	Millipore	Cat# AB5186-50UL, RRID:AB_91734
Goat anti-mouse IgG (H + L) cross-adsorbed secondary antibody, Alexa Fluor™ 488	Thermo Fisher Scientific	Cat# A-11001, RRID:AB_2534069

Goat anti-rabbit IgG (H + L) highly cross-adsorbed secondary antibody, Alexa Fluor™ 594	Thermo Fisher Scientific	Cat# A-11037, RRID:AB_2534095
Goat anti-chicken IgY (H + L) cross-adsorbed secondary antibody, Alexa Fluor™ Plus 647	Thermo Fisher Scientific	Cat# A32933, RRID:AB_2762845
Goat anti-rag IgG (H + L) cross-absorbed secondary antibody, Alexa Fluor™ 647	Thermo Fisher Scientific	Cat# A-21247 RRID:AB_141778
Media and reagents		
Precoated coverslips GG-15-1.5-PDL	Neuvitro	Cat# GG-15-PLL
VECTASHIELD® PLUS antifade mounting medium with DAPI (H-2000)	Vector Laboratories	Cat# H-2000
HBSS 1X Hanks' balanced salt solution	Gibco	Cat# 14025-092
Basal medium eagle	Gibco	Cat# 21010-046
Neurobasal medium	Thermo Fisher Scientific	Cat# 21103049
Tracers		
DBA MW3000 Alexa Fluor™488	Thermo Fisher Scientific	Cat# D34682
DBA MW3000 Texas Red™	Thermo Fisher Scientific	Cat# D3329
Fluorogold	Fluorochrome	Cat# fluoro-gold 20 mg
Chemicals		
Guangxitoxin 1E	Biotechne	Cat# 5676
Cilengitide	MedChemExpress	Cat# HY-16141
PND1186	MedChemExpress	Cat# HY-13917
Latrunculin A	Thermo Fisher Scientific	Cat# L12370
Jasplakinolide	Thermo Fisher Scientific	Cat# J7473
Cytochalasin D	Thermo Fisher Scientific	Cat# PHZ1063
Phalloidin	Thermo Fisher Scientific	Cat# P3457
Commercial assays		
MTT assay kit	Abcam	Cat# ab211091
G-actin/F-actin in vivo assay Biochem kit	Cytoskeleton Inc.	Cat# BK037
Pierce™ primary neuron isolation kit	Thermo Fisher Scientific	Cat# 88280
Experimental models: cell lines		
Hamster: CHO cells	Sesti Lab	N/A
Mouse: N2a	Sesti Lab	N/A
Organisms/strains		
Mouse: C57BL6/J background	The Jackson Laboratory	RRID:IMSR_JAX:000664
Mouse: KI *Kcnb1*^{R312H}	Genome Editing Core Facility at Rutgers	C57BL/6J-Kcnb1em1Sesf/J RRID:IMSR_JAX:037835
Mouse: KI *Kcnb1*^{NULL}	Genome Editing Core Facility at Rutgers	C57BL/6J-Kcnb1em2Sesf/J RRID:IMSR_JAX:037848
Recombinant DNA		
WT KCNB1-HA	Sesti Lab	N/A
R312H KCNB1-HA	Sesti Lab	N/A
Software and algorithms		
Neuroanatomy Fiji ImageJ	Tiago Ferreira	https://imagej.net/update-sites/neuroanatomy/
EthoVision XT	N/A	https://www.noldus.com/ethovision-xt
Colocalization Threshold Fiji ImageJ	Tony Collins	https://imagej.net/plugins/colocalization-threshold
Prism	GraphPad by Dotmatics	https://www.graphpad.com/scientific-software/prism/
Image J	NIH	https://imagej.net/software/fiji/
NIS elements	Nikon Instrument Inc.	https://www.microscope.healthcare.nikon.com/products/software/nis-elements
Olympus Fluoview	Olympus Life Science	https://www.olympus-lifescience.com/en/landing/fv_technologies/

Animals

Wild type (C57BL6/J) and homozygote *knockin* (KI) C57BL/6J-*Kcnb1*^{em1Sesf}/J and C57BL/6J-*Kcnb1*^{em2Sesf}/J of either sex at developmental stages: E13 and 3 months were used. The C57BL/6J-*Kcnb1*^{em1Sesf}/J mouse, here named *Kcnb1*^{R312H} mouse, bears a mutated allele that causes an arginine at position 312 in the voltage-sensor of the protein (S4 transmembrane segment), to be replaced by histidine. The C57BL/6J-*Kcnb1*^{em2Sesf}/J mouse, here called the *Kcnb1*^{NULL} mouse, bears a mutated allele that contains a stop sequence after serine 336 in the voltage-sensor domain. The resulting truncated Kcnb1 protein is degraded and does not traffic to the plasma membrane[2]. Three months old KI animals have normal body weight (males weight: WT = 29.2 ± 1.1 gr; *Kcnb1*$^{R312H(+/+)}$ 29.4 ± 1.0 gr and *Kcnb1*$^{NULL(+/+)}$ 29.4 ± 1.1 gr; females: WT = 26.1 ± 1.0 gr; *Kcnb1*$^{R312H(+/+)}$ 25.6 ± 0.8 gr and *Kcnb1*$^{NULL(+/+)}$ 25.9 ± 0.9 gr) and size. Littermates of either sex were randomly assigned to experimental groups. All experiments with animals performed in this study were approved by the Rutgers University Institutional Animal Care and Use Committee (IACUC, protocol # PROTO999900293). We have complied with all relevant ethical regulations for animal use.

Behavioral protocols

Digital ventilated cage (DVC®). The DVC® rack is a monitoring system that tracks the animal's locomotor activity and well-being via 12

capacitance-sensing electrodes positioned on the cage's floor. Single-housed three-month-old mice were acclimated to the new environment (single-cage) for a week and then their activity was recorded over a week. Mice were subject to a 12–12 h light/dark cycle with the dark period starting at 18 h (6 pm) and ending at 6 h (6 am). The DVC system provided the average distance walked in a day, the cumulative distance walked in a week, and the animal locomotion index, which is based on activation density whereby a capacitive electrode is triggered by the animal when the difference between two consecutive readings exceeds a predetermined threshold (λ)[79]. The λ threshold allows to filter out the noise due to capacitance fluctuations from signals resulting from animal movements.

Dead reckoning. The path integration (dead reckoning) test apparatus consisted of a walled circular arena (1 m in diameter) covered with a plastic layer to allow 70% ethanol disinfection after each trial and a digital camera positioned on top of the apparatus. The arena was placed in a visual cues-free dark room. At the beginning of each trial, a single-housed mouse and its shelter and bedding were transferred from the housing cage to the lower right end of the arena. Then, the animal was allowed 15 min to explore the arena while the experimenter left the room. Then, the animals and their bedding were taken out of the apparatus and returned to the home cage. The arena was cleaned with 70% ethanol and the recordings were analyzed with Noldus EthoVision XT software.

Hanging test. The mouse was placed on a 30 × 30 cm metal grid, and a soft bedding material was positioned underneath the setup to guarantee a soft landing. Three seconds were given to allow the mouse to obtain a solid grip. Then, the grid was inverted and the latency to fall was measured with a chronometer by two evaluators. Maximum time was set at 120 s and single trial results were averaged with each other. The grid was cleaned with 70% ethanol and the soft bedding was replaced after each trial.

Visual looming test. A mouse was placed in an arena composed of 40 cm × 40 cm × 30 cm white PVC panels in a soundproofed room devoid of any visual cue and lightened under dim white LED light. An opaque shelter was placed in the top right corner of the arena, with the entrance facing the center of the arena. A screen was positioned on top of the arena, along with a digital camera which recorded the activity of the animal for the entire duration of the test. The mouse was allowed to acclimatize to the arena for 15 min with the screen displaying a white background. The stimulus consisted of an expanding black circle originating from the center of the screen. The mouse's reactions to the stimulus were scored as follows: (−1) freezing (1), fleeing, or (0) no response. The arena was cleaned with 70% ethanol between each trial[80].

Startle reflex. The mouse was placed into the same arena used for the visual looming test and allowed to acclimate for 15 as described. The stimulus consisted of a 100 dB sound lasting for 0.5 s. Reactions were scored as follows: (0) No response (1), sound acknowledgment (2), shaking (3), brief startle (4), slight movement[5], and jumping. The arena was cleaned with 70% ethanol between each trial.

Marble burying. The mouse was placed in a clean conventional-sized cage, prepared with 3 cm of clean bedding. The cage was provided with 8 evenly spaced 14 mm diameter glass marbles. After 30 min, the animal was removed, and the cage was photographed. Three evaluators counted the number of marbles that were covered by bedding for at least two-thirds of their size. After each trial, the marbles and cage were cleaned with 70% ethanol, while the bedding was discarded.

Nesting building test. The mouse was placed in a clean, enrichment-free, conventional-sized cage, and was provided with a fresh pad of nesting material that was weighed before the beginning of the trial. After 16 h, a picture of the nest was taken. Unused untorn nestlets were let dry for 1 h at room temperature to remove potential humidity caused by urine, and the final weight was measured using a digital scale. The percentage of torn nesting material was obtained by comparing the weight of the final nestlet to the initial one. The nest was scored from 1 to 5 according to the guidelines of nest building score[81].

Visual cliff. The mouse was placed into an arena composed of 40 cm × 40 cm × 30 cm white PVC panels, while the bottom was a transparent PVC panel. Underneath the arena, a checkered board was placed, designed in a way to give the illusion of a cliff. Mice were continuously recorded with a digital camera for 15 min. The amount of time spent on the close-by side was measured with a chronometer by two evaluators. Single-trial results were averaged with each other, and % of time spent in the nearby area was calculated. The arena was cleaned with 70% ethanol between each trial.

Cell cultures

Chinese hamster ovary cells. Chinese hamster ovary K1 (CHO) cells were incubated in 95% air and 5% CO_2 at 37 °C. The cells were seeded at a density of 0.5 million cells/mL using a hemocytometer and maintained in Dulbecco Modified Eagle's medium as described. Once confluence was reached, cells were harvested using Trypsin and seeded as previously described.

Mouse neuroblastoma cells. Undifferentiated mouse neuroblastoma (N2a) cells were incubated in 95% air and 5% CO_2 at 37 °C. The cells were seeded at a density of 0.5 million cells/mL using a hemocytometer and maintained in Dulbecco Modified Eagle's medium as described. Once confluence was reached, cells were harvested using Trypsin and seeded as previously described.

Primary cortical neurons. Experiments involving primary cortical neurons were performed without prior knowledge of the genotype. A pregnant dam at 13 days post-fertilization (E13) was euthanized by CO_2 followed by cervical dislocation. Cortical tissue from individual embryos was mechanically triturated under a dissecting microscope in ice-cold sterile Hank's Balanced Salt Solution (HBSS) using tweezers. The tissue was transferred into a 1.7 mL Eppendorf tube, the extra HBSS was gently removed and 100.0 µL of primary neuron isolation kit solution with papaine was added. The tissue was incubated for 30 min at 37 °C in a water bath. After incubation, the dissociated cells were centrifuged with a mini centrifuge for 15 s and washed twice with 1.0 mL HBSS. Then, the cells were resuspended in 1.0 mL neuronal plating media (for 20 mL: 18.31 mL of Basal Medium Eagle + Earle's Salts, supplemented with 1.0 mL of heat-inactivated fetal bovine serum FBS, 200 µL of sodium pyruvate from a 100× stock, 200 µL of glutamine from a 200 nM stock, and 100 µL of penicillin/streptomycin from a 200× stock). Cells were counted with a Neubauer counting chamber and plated in 12 mm poly-d-lysine-precoated Petri dishes (GG-12-1.5-PDL, Neuvitro, Camas, WA) at a density of ~100,000 cells/dish in 1.5 mL plating media/dish. Cultures were maintained in the plating medium at 37 °C in 95% air and 5% CO_2 for 24 h. Then, the plating medium was removed and replaced with Neurobasal medium. Tail samples from individual embryos were processed for genotyping.

Biochemistry

Western blotting, immunofluorescence, and analyses were performed without prior knowledge of the genotype.

Crude brain and cortical lysates. Animals were euthanized by asphyxiation using CO_2 followed by cervical dislocation. The brain was extracted from the skull and the layer of meninges and blood vessels was removed with forceps. Crude brain lysates were obtained by symmetrical

sagittal sectioning of the tissue across the midline. For cortical lysates, the brain was maintained in PBS and the cortex was dissected under a stereo microscope. Half-brains or half-cortices were initially homogenized using a plastic tissue grinder in a 1.7 mL conical tube containing lysis buffer (0.32 M sucrose, 5 mM Tris-Cl pH 6.8, 0.5 mM EDTA) and protease inhibitor cocktail (Sigma-Aldrich). Further homogenization of the tissue was obtained by sonication of the sample for 1–3 min in iced water. Brain homogenized was centrifuged for 10 min at 14,000 rpm at 4 °C. The supernatant was collected and stored at −80 °C for further analysis.

Western blotting. For Western blot analysis, protein content was initially quantified via Bradford colorimetric assay (Sigma Aldrich). The samples were prepared into 1.7 mL conical tubes, with 40–100 µg of protein. Samples were diluted in 5× sample buffer (Sodium dodecyl sulfate (SDS) 10%; Bromophenol blue 0.02%; glycerol 30%; Tris-HCL 0.5 M) and 2–5% Beta-mercaptoethanol (Sigma Aldrich) was added. Samples were heated at 95–100 °C for 5 min, centrifuged at 10,000 RPM for 1 min, and resuspended using a pipette to allow homogeny suspension of protein into the media. The proteins were resolved in 10–15% SDS-PAGE depending on the molecular weight of the protein of interest, and successively transferred into a nitrocellulose membrane. Membranes were washed once in Tris Buffer Saline (TBS) and then blocked in a 5% solution of nonfat dry milk in Tris Buffered Saline with Tween® 20 (TBST) for 1 h at room temperature on an orbital shaker at 50 RPM. Membranes were stained with the primary antibody diluted at 1:1000 at 4 °C on an orbital shaker overnight at 50 RMP. Membranes were washed three times 10 min each with TBST, and sequentially incubated with a secondary antibody (goat anti-rabbit IgG antibody, (H + L) HRP conjugate or anti-mouse IgG antibody, dilution 1:4000) for 1 h at room temperature on an orbital shaker at 50 RPM. Membranes were washed three times 10 min in TBST and exposed in ChemiDoc MP (Bio-Rad) using SuperSignal™ West Pico PLUS Chemiluminescent Substrate (ThermoFischer).

Tracer injection. The animals were anesthetized with 4–5% isoflurane in 100% O_2 and titrated to effect (maintenance 2% isoflurane). After induction, the mouse was placed into the Kopf stereotaxic frame. Prior to making an incision, analgesia was further provided by subcutaneous injection of 0.025% Buprivicaine. The tracers were dissolved in saline solution (0.9% NaCl) and were injected with an automatic pressure injector. To avoid backflow, the needle was maintained for 5 min prior, to and 10 min after, the injection of the tracer. Fluorogold (retrograde), was injected into the thalamus at the following coordinates: Mid: +1.2 mm, Bregma: −1.06 mm, Top: −4.0 mm. BDA MW3000 Alexa 488 (anterograde), was injected into the cortex at the following coordinates: Mid: −1.2 mm, Bregma: −0.6 mm, Top: −1.0 mm. BDA MW3000 Texas red (anterograde), was injected into the thalamus at the following coordinates: Mid: +1.2 mm, Bregma: −1.06 mm, Top: −4.0 mm according to the Mouse brain atlas[82]. After surgery, the animals were monitored for any veterinary signs. Monitoring was daily for the first 3 days or until nest building begins (typically, if delayed nest building begins 4–6 days post-surgery).

Adult brains imaging. Anesthetized mice (a cocktail of 100 mg/kg ketamine and 10 mg/kg xylazine injected intraperitoneally) were cleared with 0.9% filtered NaCl and then perfused with room temperature 4% paraformaldehyde solutions. The mice were decapitated, and their brains were extracted and post-fixed in 4% paraformaldehyde overnight at 4 °C. The brain was washed twice with PBS and cryoprotected using a sucrose gradient. Thus, the brain was immersed in 10% sucrose at 4 °C until completely sunk. This step was repeated in 20% and 30% sucrose. Then, the brain was fast-frozen by slow immersion in isopentane pre-cooled at −20 °C, that was maintained in thermal contact with dry ice. Brain slices were cut 50 µm thick throughout the cortex and the hippocampus in a 1:20 series, so that the same set of tissue samples could be used for expression of different makers. When required, tissues were permeabilized in 0.1% Triton-X in PBS for 7 min. Free-floating sections were processed for double or triple labeling with primary antibodies. After 24–48 h of incubation at 4 °C in primary antibodies, sections were washed three times with PBS for 10 min and incubated with the appropriate secondary conjugated antibody. After 1 h at room temperature, sections were washed three times with PBS. Slices were mounted on a Superfrost slide and mounting VECTASHIELD Antifade Mounting Medium with DAPI mounting buffer (Vector Laboratories, Burlingame, CA) was applied. Slices were cover-slipped and sealed with nail polish.

Connectivity heat maps. The process used to construct heat maps is illustrated in Video S1. Briefly, heat maps were constructed by coloring and Z-stacking 30 coronal brain maps from the Mouse brain atlas, corresponding to progressive coronal brain sections. Each interested area of a map was colored according to the density of the projections expressed in percent. The green color was assigned when 66–100% of the samples had projections in a given area; the yellow color was 33–65% and the red color was 0–32% (blue color is the site of injection).

Primary neurons staining. Neurons were fixed using a solution of 50% methanol, and 50% acetone and kept for 20 min on dry ice. Neurons were washed three times with PBS (10 min for each wash) and blocked for 1 h at room temperature with 3% BSA in PBS 1×. After 24 h of incubation at 4 °C in primary antibodies diluted in 3% BSA in PBS 1×, neurons were washed three times with PBS (10 min each wash). Washes were followed by the application of the appropriate secondary fluorophore-conjugated antibodies. Secondary antibodies were kept on neurons for 1 h at room temperature. Neurons were washed three times with PBS (10 min each wash). Coverslips were rotated to allow neurons to face the inside of the slide and mounted on a microscope slide with VECTASHIELD Antifade Mounting Medium with DAPI mounting buffer (Vector Laboratories, Burlingame, CA) and stored at 4 °C. Staining was visualized with a Zeiss Axiophot microscope or with an Olympus FV1000MPE (Orangeburg, NY) multi-photon microscope or Nikon Eclipse Ti2 series (Tokyo, Japan) confocal microscope, all equipped with dedicated software.

In vitro assays

In vitro experiments were performed without prior knowledge of the genotype.

Pharmaceutical compounds and toxins were freshly diluted from stocks and added to the medium at the indicated concentrations. In primary neuronal cultures, compounds were added to the medium on DIV2 and supplemented until the end of the experiment.

Proliferation assay. CHO cells were plated at a concentration of ~10,000 cells/well into 96-well tissue culture plates. Twenty-four hours after seeding, cells were transfected with various plasmids using Lipofectamine 2000 diluted in OPTI transfection medium. Two days post-transfection, the number of viable cells was assessed using the microtiter-plate colorimetric MTT assay. Briefly, the cell's growing media was replaced with MTT reagent diluted into serum-free media following the manufacturer's protocol. After 3 h incubation at 37 °C, the MTT solvent was added. Cells were incubated on a shaker at 37 °C for 15 min, and measurements were obtained using a Tecan Infinite M200pro (Männedorf, Switzerland) microplate reader at an absorbance of 590 nm.

Neurite outgrowth. N2a cells were plated at a concentration of ~100,000 cells/well into 6-well tissue culture plates. Forty-eight hours after seeding, cells were transfected with various plasmids using Lipofectamine 2000 diluted in OPTI transfection medium. GFP plasmid was co-transfected to evidence cells positive from the transfection. Forty-eight hours after transfection, N2a cells were photographed with a Zeiss Axiovert 200 M microscope equipped with a GFP lamp. The neurite (the

longer one in multineuritic cells) of GFP-fluorescent cells was measured using ImageJ 1.52a software.

Electrophysiology. Data were recorded with an Axopatch 200B (Molecular Devices, San Jose, CA), a PC (Dell, Round Rock, TX), equipped with Clampex software (Molecular Devices, San Jose, CA), filtered at $f_c = 1$ kHz and sampled at 3.0 kHz. An Ag-AgCl electrode connected to the bath solution using a KCl-agar bridge was used as a reference. Pipette solution was (in mM): 135.0 K-gluconate, 4.0 KCl, 4.0 MgATP, 0.3 Na3GTP, 10.0 HEPES (buffered to pH = 7.4 with KOH). Bath solution (in mM) was artificial cerebrospinal fluid (aCSF) with the pH and oxygen level stabilized by bubbling with 5% CO_2 and 95% O_2: 125.0 NaCl, 3.0 KCl, 2.5 $CaCl_2$, 1.3 $MgSO_4$ 1.3 NaH_2PO_4 26.0 $NaHCO_3$ 13.0 mM D-glucose. Pipettes (~5 MΩ) were obtained by pulling borosilicate glass with a Sutter P-97 puller (Sutter Instruments, Novato, CA). Whole-cell currents were elicited by 0.5 s voltage sweeps from a holding potential of −80 mV to 80 mV in 20 mV increments and leak subtraction (if needed) was performed digitally using Clampfit software (molecular devices). Macroscopic conductance (G) curves were calculated as:

$$G(V) = \frac{I_s}{V - V_{rev}} \tag{1}$$

where I_s the macroscopic current at steady-state (at the end of the voltage pulse) and V_{rev} is the reversal potential. V_{rev}, was estimated to be ≈−70 mV, for WT and *Kcnb1*$^{R312H(+/+)}$ currents, based on current-clamp measurements and estimates of offset potentials, including series resistance (offset potentials were not compensated for when generating current-voltage relationships). G/G_{Max} curves were fitted to the function:

$$\frac{G(V)}{G_{Max}} = \frac{1}{1 + EXP\left[\left(V_{1/2} - V\right)/V_S\right]} \tag{2}$$

where V is the membrane voltage, $V_{1/2}$ is the value of the voltage at which Eq. 2 is equal to 0.5 and V_S is the slope coefficient (in mV). For noise-variance analysis, currents were evoked by $M = 10$–20 consecutive voltage jumps from a holding voltage of −80 mV to 40 mV for 0.5 s. The mean-variance, σ^2, was calculated as:

$$M\sigma^2 = \sum_{i=1,M} \left(I_i - I\right)^2 \tag{3}$$

where I is the mean macroscopic current:

$$MI = \sum_{i=1,M} I_i \tag{4}$$

The single-channel current, i, and the number of channels in the cell, N_c, were estimated by fitting the following relationship (I_0 is a constant):

$$\sigma^2 = i\left(I - I_0\right) - \left(I - I_0\right)^2/N_c \tag{5}$$

The open probability, p_o, was calculated as:

$$p_o = \frac{I}{iN_c} \tag{6}$$

For recording the activity of neurons, cells were clamped in the current clamp, and APs were elicited by current injections from −10 pA to 120 pA in 10 pA increments. Cells with a resting membrane potential ≥ −40 mV were discharged. At the end of each recording, the cell cytoplasm was gently sucked into the patch pipette, to quantify *Kcnb1* and *VGluT1* transcripts by using a modified protocol of the polymerase chain reaction (PCR) analysis of gene expression in single neurons technique of the patch clamp[28]. Briefly, the cell was patched with a sterile RNase-free pipette. After the recording, the patch pipette containing the cell's cytoplasm was transferred to a PCR tube for real-time-PCR analysis, using a micropipette ejector and a micro-centrifuge according to the manufacturer's instructions. The cell content was diluted in 10 µL lysis/DNase solution and then RT mix was added to perform the reverse transcription reaction. Then, the RT-PCR amplification was carried out and analyzed.

Recovery after photobleaching (FRAP). E13 pure primary neuron cultures at DIV13 were transfected with 20 µL of transfection reagent and 1.5 µg of plasmid DNA was used for each transfection. Cells were transfected with Lipofectamine and incubated for 16 h prior to FRAP, using an Olympus FV1000MPE 2-photon microscope. Twenty images were taken every 0.5 s (2 Hz). Three images were taken pre-bleaching for control. Photobleaching was performed at 1.5 s and the first image after photobleaching was taken at 2 s. Measurements were taken in basal dendrites (where Kcnb1 expression, along with the soma is maximal[83]), at a distance from the soma (~5–15 µm) that we tried to maintain constant as much as possible. We kept photobleaching settings constant and controls were repeated every experimental session. The fluorescence recovery, $R(t)$, was calculated as:

$$R(t) = 100\frac{F - F_{min}}{F_{Max} - F_{min}} \tag{7}$$

and is expressed in *percent*. Fluorescence recovery was assumed to be reaction-limited and was fitted to a single exponential function:

$$R(t) - 1 - e^{-k_{off}t} \tag{8}$$

where k_{off} is the rate of unbinding of Lifeact-GFP to F-actin[53]. FRAP measurements in dendrites in which the recovery varied less than 10% were discarded.

Statistics and reproducibility

Sample size, N, was estimated with power analysis with $\alpha = 0.05$ and power = 0.8[84]. Normality and log-normality tests (D' Agostino and Pierson) were calculated for normal distribution. Significance, P, was assumed to be at the 95% confidence limit or greater. Significance was estimated with one-way ANOVA with a Tukey's post hoc test, a two-tailed student t-test, or a two-sample Kolmogorov–Smirnov test, using Prism software. Data are presented as mean ± standard error of the mean.

Data availability

All data generated or analyzed during this study, including the source data behind the figures in the paper, are available at Dryad at: https://doi.org/10.5061/dryad.gmsbcc2ws. All other data are available from the corresponding author upon reasonable request.

Received: 26 June 2024; Accepted: 2 December 2024;
Published online: 30 December 2024

References

1. Forzisi, E. & Sesti, F. Non-conducting functions of ion channels: the case of integrin-ion channel complexes. *Channels* **16**, 185–197 (2022).
2. Bortolami, A. et al. Integrin-KCNB1 potassium channel complexes regulate neocortical neuronal development and are implicated in epilepsy. *Cell Death Differ* **30**, 687–701 (2022).
3. McCord, M. C. & Aizenman, E. Convergent Ca2+ and Zn2+ signaling regulates apoptotic Kv2.1 K+ currents. *Proc. Natl. Acad. Sci. USA* **110**, 13988–13993 (2013).
4. Scheffer, I. E. et al. ILAE classification of the epilepsies: position paper of the ILAE commission for classification and terminology. *Epilepsia* **58**, 512–521 (2017).

5. de Kovel, C. G. F. et al. Neurodevelopmental disorders caused by de novo variants in KCNB1 genotypes and phenotypes. *JAMA Neurol.* **74**, 1228–1236 (2017).
6. Bar, C. et al. Expanding the genetic and phenotypic relevance of KCNB1 variants in developmental and epileptic encephalopathies: 27 new patients and overview of the literature. *Hum. Mutat.* **41**, 69–80 (2020).
7. Bar, C. et al. Developmental and epilepsy spectrum of KCNB1 encephalopathy with long-term outcome. *Epilepsia* **61**, 2461–2473 (2020).
8. Hiraide T. et al. A novel de novo KCNB1 variant altering channel characteristics in a patient with periventricular heterotopia, abnormal corpus callosum, and mild seizure outcome. *J. Hum. Genet.* **68**, 1–7 (2022).
9. Púa-Torrejón, R. C. et al. [Variability of the clinical expression of KCNB1 encephalopathy]. *Rev. Neurol.* **73**, 403–408 (2021).
10. Veale, E. L., Golluscio, A., Grand, K., Graham, J. M. & Mathie, A. A KCNB1 gain of function variant causes developmental delay and speech apraxia but not seizures. *Front. Pharm.* **13**, 1093313 (2022).
11. Lu, J. M., Zhang, J. F., Ji, C. H., Hu, J. & Wang, K. Mild phenotype in a patient with developmental and epileptic encephalopathy carrying a novel de novo KCNB1 variant. *Neurol. Sci.* **42**, 4325–4327 (2021).
12. Specchio, N. & Curatolo, P. Developmental and epileptic encephalopathies: what we do and do not know. *Brain* **144**, 32–43 (2021).
13. McTague, A., Howell, K. B., Cross, J. H., Kurian, M. A. & Scheffer, I. E. The genetic landscape of the epileptic encephalopathies of infancy and childhood. *Lancet Neurol.* **15**, 304–316 (2016).
14. Kang, S. K. et al. Altered neurological and neurobehavioral phenotypes in a mouse model of the recurrent KCNB1-p.R306C voltage-sensor variant. *Neurobiol. Dis.* **194**, 106470 (2024).
15. Hawkins, N. A. et al. Epilepsy and neurobehavioral abnormalities in mice with a dominant-negative KCNB1 pathogenic variant. *Neurobiol. Dis.* **147**, 105141 (2021).
16. Jirkof, P. Burrowing and nest building behavior as indicators of well-being in mice. *J. Neurosci. Methods* **234**, 139–146 (2014).
17. Albelda, N. & Joel, D. Animal models of obsessive-compulsive disorder: exploring pharmacology and neural substrates. *Neurosci. Biobehav Rev.* **36**, 47–63 (2012).
18. Crawley, J. N. Behavioral phenotyping of transgenic and knockout mice: experimental design and evaluation of general health, sensory functions, motor abilities, and specific behavioral tests. *Brain Res.* **835**, 18–26 (1999).
19. Etienne, A. S. & Jeffery, K. J. Path integration in mammals. *Hippocampus* **14**, 180–192 (2004).
20. Yang, X. et al. A simple threat-detection strategy in mice. *BMC Biol.* **18**, 93 (2020).
21. Lee, Y. & Davis, M. Role of the hippocampus, the bed nucleus of the stria terminalis, and the amygdala in the excitatory effect of corticotropin-releasing hormone on the acoustic startle reflex. *J. Neurosci.* **17**, 6434–6446 (1997).
22. Medford, N. & Critchley, H. D. Conjoint activity of anterior insular and anterior cingulate cortex: awareness and response. *Brain Struct. Funct.* **214**, 535–549 (2010).
23. Gorny, J. H., Gorny, B., Wallace, D. G. & Whishaw, I. Q. Fimbria-Fornix lesions disrupt the dead reckoning (Homing) component of exploratory behavior in mice. *Learn Mem.* **9**, 387–394 (2002).
24. Speca, D. J. et al. Deletion of the Kv2.1 delayed rectifier potassium channel leads to neuronal and behavioral hyperexcitability. *Genes Brain Behav.* **13**, 394–408 (2014).
25. Staley, K. Molecular mechanisms of epilepsy. *Nat. Neurosci.* **18**, 367–372 (2015).
26. Bortolami, A. & Sesti, F. Ion channels in neurodevelopment: lessons from the Integrin-KCNB1 channel complex. *Neural Regen. Res.* **18**, 2365–2369 (2023).
27. Yu, W., Shin, M. R. & Sesti, F. Complexes formed with integrin-alpha5 and KCNB1 potassium channel wild type or epilepsy-susceptibility variants modulate cellular plasticity via Ras and Akt signaling. *FASEB J.* **33**, 14680–14689 (2019).
28. Monyer, H. & Jonas, P. Polymerase chain reaction analysis of ion channel expression in single neurons of brain slices. In *Single-Channel Recording [Internet]* (ed. Sakmann, B. & Neher, E.) 357–373 (Springer, Boston, 2023). https://doi.org/10.1007/978-1-4419-1229-9_16.
29. Sigworth, F. J. The variance of sodium current fluctuations at the node of Ranvier. *J. Physiol.* **307**, 97–129 (1980).
30. Fernández-Mariño, A. I. et al. Inactivation of the Kv2.1 channel through electromechanical coupling. Nature **622**, 410–417 (2023).
31. Herrington, J. et al. Blockers of the delayed-rectifier potassium current in pancreatic beta-cells enhance glucose-dependent insulin secretion. *Diabetes* **55**, 1034–1042 (2006).
32. Bishop, H. I. et al. Distinct cell- and layer-specific expression patterns and independent regulation of Kv2 channel subtypes in cortical pyramidal neurons. *J. Neurosci*. https://pubmed.ncbi.nlm.nih.gov/26538660/ (2015).
33. Luebke, J. I. et al. Age-related changes to layer 3 pyramidal cells in the rhesus monkey visual cortex. *Cereb. Cortex* **25**, 1454–1468 (2015).
34. Barker-Haliski, M. & White, H. S. Glutamatergic mechanisms associated with seizures and epilepsy. *Cold Spring Harb. Perspect. Med.* **5**, a022863 (2015).
35. Erlander, M. G., Tillakaratne, N. J. K., Feldblum, S., Patel, N. & Tobin, A. J. Two genes encode distinct glutamate decarboxylases. *Neuron* **7**, 91–100 (1991).
36. Chapman, E. R., An, S., Barton, N. & Jahn, R. SNAP-25, a t-SNARE which binds to both syntaxin and synaptobrevin via domains that may form coiled coils. *J. Biol. Chem.* **269**, 27427–27432 (1994).
37. Fremeau, R. T. et al. The expression of vesicular glutamate transporters defines two classes of excitatory synapse. *Neuron* **31**, 247–260 (2001).
38. Ni, B., Wu, X., Yan, G. M., Wang, J. & Paul, S. M. Regional expression and cellular localization of the Na(+)-dependent inorganic phosphate cotransporter of rat brain. *J. Neurosci.* **15**, 5789–5799 (1995).
39. Choi, D. W. Excitotoxic cell death. *J. Neurobiol.* **23**, 1261–1276 (1992).
40. Shepherd, G. M. G. & Yamawaki, N. Untangling the cortico-thalamo-cortical loop: cellular pieces of a knotty circuit puzzle. *Nat. Rev. Neurosci.* **22**, 389–406 (2021).
41. Hofman, J., Hutny, M., Sztuba, K. & Paprocka, J. Corpus callosum agenesis: an insight into the etiology and spectrum of symptoms. *Brain Sci.* **10**, 625 (2020).
42. Ross, D. T., Meaney, D. F., Sabol, M. K., Smith, D. H. & Gennarelli, T. A. Distribution of forebrain diffuse axonal injury following inertial closed head injury in miniature swine. *Exp. Neurol.* **126**, 291–298 (1994).
43. Kim, J. Y. et al. HDAC1 nuclear export induced by pathological conditions is essential for the onset of axonal damage. *Nat. Neurosci.* **13**, 180–189 (2010).
44. Manders, E. M. M., Verbeek, F. J. & Aten, J. A. Measurement of co-localization of objects in dual-colour confocal images. *J. Microsc.* **169**, 375–382 (1993).
45. Chou, F. S. & Wang, P. S. The Arp2/3 complex is essential at multiple stages of neural development. *Neurogenesis* **3**, e1261653 (2016).
46. Flynn, K. C. The cytoskeleton and neurite initiation. *Bioarchitecture* **3**, 86–109 (2013).
47. Webb, D. J., Zhang, H., Majumdar, D. & Horwitz, A. F. alpha5 integrin signaling regulates the formation of spines and synapses in hippocampal neurons. *J. Biol. Chem.* **282**, 6929–6935 (2007).
48. Shi, Y. & Ethell, I. M. Integrins control dendritic spine plasticity in hippocampal neurons through NMDA receptor and Ca2+/calmodulin-dependent protein kinase II-mediated actin reorganization. *J. Neurosci.* **26**, 1813–1822 (2006).

49. Kumar, V., Zhang, M. X., Swank, M. W., Kunz, J. & Wu, G. Y. Regulation of dendritic morphogenesis by Ras-PI3K-Akt-mTOR and Ras-MAPK signaling pathways. *J. Neurosci.* **25**, 11288–11299 (2005).
50. Clegg, D. O., Wingerd, K. L., Hikita, S. T. & Tolhurst, E. C. Integrins in the development, function and dysfunction of the nervous system. *Front Biosci.* **8**, d723–d750 (2003).
51. Lilja, J. & Ivaska, J. Integrin activity in neuronal connectivity. *J. Cell Sci.* **131**, jcs212803 (2018).
52. Schmid, R. S. & Anton, E. S. Role of integrins in the development of the cerebral cortex. *Cereb. Cortex* **13**, 219–224 (2003).
53. Cai, N. et al. Recent advances in fluorescence recovery after photobleaching for decoupling transport and kinetics of biomacromolecules in cellular physiology. *Polymers* **14**, 1913 (2022).
54. Riedl, J. et al. Lifeact: a versatile marker to visualize F-actin. *Nat. Methods* **5**, 605–607 (2008).
55. Pankov, R. & Yamada, K. M. Fibronectin at a glance. *J. Cell Sci.* **115**, 3861–3863 (2002).
56. Kapp, T. G. et al. A comprehensive evaluation of the activity and selectivity profile of ligands for RGD-binding integrins. *Sci. Rep.* **7**, 39805 (2017).
57. Giancotti, F. G. Complexity and specificity of integrin signalling. *Nat. Cell Biol.* **2**, E13–E14 (2000).
58. Yu, W., Gowda, M., Sharad, Y., Singh, S. A. & Sesti, F. Oxidation of KCNB1 potassium channels triggers apoptotic integrin signaling in the brain. *Cell Death Dis.* **8**, e2737 (2017).
59. Alberts, B. et al. *Molecular Biology of the Cell* 4th edn (Garland Science, 2002).
60. de Kovel, C. G. et al. Targeted sequencing of 351 candidate genes for epileptic encephalopathy in a large cohort of patients. *Mol. Genet. Genom. Med.* **4**, 568–580 (2016).
61. Medlin, L. C., Bello-Espinosa, L. & MacAllister, W. S. Neuropsychological profiles of two patients with differing SCN8A-pathogenic variants. *Appl. Neuropsychol. Child* **11**, 561–566 (2022).
62. Bocksteins, E. & Snyders, D. J. Electrically silent Kv subunits: their molecular and functional characteristics. *Physiology* **27**, 73–84 (2012).
63. McCrossan, Z. A. et al. MinK-related peptide 2 modulates Kv2.1 and Kv3.1 potassium channels in mammalian brain. *J. Neurosci.* **23**, 8077–8091 (2003).
64. Zheng, H., Liu, W., Anderson, L. Y. & Jiang, Q. X. Lipid-dependent gating of a voltage-gated potassium channel. *Nat. Commun.* **2**, 250 (2011).
65. Liu, J. S. Molecular genetics of neuronal migration disorders. *Curr. Neurol. Neurosci. Rep.* **11**, 171–178 (2011).
66. Wong, M. Stabilizing dendritic stucture as a novel therapeutic approach for epilepsy. *Expert Rev. Neurother.* **8**, 907–915 (2008).
67. Gardiner, J. & Marc, J. Disruption of normal cytoskeletal dynamics may play a key role in the pathogenesis of epilepsy. *Neuroscientist* **16**, 28–39 (2010).
68. Muñoz-Lasso, D. C., Romá-Mateo, C., Pallardó, F. V. & Gonzalez-Cabo, P. Much more than a scaffold: cytoskeletal proteins in neurological disorders. Cells. https://www.ncbi.nlm.nih.gov/pmc/articles/PMC7072452/ (2020).
69. da Silva, J. S. & Dotti, C. G. Breaking the neuronal sphere: regulation of the actin cytoskeleton in neuritogenesis. *Nat. Rev. Neurosci.* **3**, 694–704 (2002).
70. Lin, C. H. & Forscher, P. Cytoskeletal remodeling during growth cone-target interactions. *J. Cell Biol.* **121**, 1369–1383 (1993).
71. O'Connor, T. P. & Bentley, D. Accumulation of actin in subsets of pioneer growth cone filopodia in response to neural and epithelial guidance cues in situ. *J. Cell Biol.* **123**, 935–948 (1993).
72. Meberg, P. J. & Bamburg, J. R. Increase in neurite outgrowth mediated by overexpression of actin depolymerizing factor. *J. Neurosci.* **20**, 2459–2469 (2000).
73. Derlig, K. et al. Simiate is an actin binding protein involved in filopodia dynamics and arborization of neurons. *Front. Cell Neurosci.* **8**, 99 (2014).
74. Bentley, D. & Toroian-Raymond, A. Disoriented pathfinding by pioneer neurone growth cones deprived of filopodia by cytochalasin treatment. *Nature* **323**, 712–715 (1986).
75. Forscher, P. & Smith, S. J. Actions of cytochalasins on the organization of actin filaments and microtubules in a neuronal growth cone. *J. Cell Biol.* **107**, 1505–1516 (1988).
76. Murakoshi, H., Shi, G., Scannevin, R. H. & Trimmer, J. S. Phosphorylation of the Kv2.1 K+ channel alters voltage-dependent activation. *Mol. Pharm.* **52**, 821–828 (1997).
77. Park, K. S., Mohapatra, D. P., Misonou, H. & Trimmer, J. S. Graded regulation of the Kv2.1 potassium channel by variable phosphorylation. *Science* **313**, 976–979 (2006).
78. Sobko, A., Peretz, A. & Attali, B. Constitutive activation of delayed-rectifier potassium channels by a src family tyrosine kinase in Schwann cells. *EMBO J.* **17**, 4723–4734 (1998).
79. Iannello, F. Non-intrusive high throughput automated data collection from the home cage. *Heliyon*. https://www.cell.com/heliyon/abstract/S2405-8440(18)38472-X (2019).
80. Koehler, C. C., Hall, L. M., Hellmer, C. B. & Ichinose, T. Using looming visual stimuli to evaluate mouse vision. *J. Vis. Exp*. https://doi.org/10.3791/59766 (2019).
81. Deacon, R. M. Measuring motor coordination in mice. *J. Vis. Exp.* **29**, e2609 (2013).
82. *Paxinos and Franklin's the Mouse Brain in Stereotaxic Coordinates [Internet]*. https://shop.elsevier.com/books/paxinos-and-franklins-the-mouse-brain-in-stereotaxic-coordinates/paxinos/978-0-12-816157-9 (2019).
83. Maletic-Savatic, M., Lenn, N. & Trimmer, J. Differential spatiotemporal expression of K+ channel polypeptides in rat hippocampal neurons developing in situ and in vitro. *J. Neurosci.* **15**, 3840–3851 (1995).
84. Noordzij, M. et al. Sample size calculations: basic principles and common pitfalls. *Nephrol. Dial. Transpl.* **25**, 1388–1393 (2010).

Acknowledgements

We thank Drs. Guido Gottardo, Stefano Gaburro, Matthew Keller, and Jeetendra Eswaraka for help with the DCV system, Yong Kim and Clara Berdasco for help with the ultracentrifuge, and Cooper Brennan with help with the CHO cells. This work was supported by an NIA grant (R01AG060919) an NSF grant (2030348) to F.S. and a NJ Governor's Council for Medical Research and Treatment of Autism predoctoral fellowship (CAUT23AFP015) to A.B.

Author contributions

A. Bortolami performed literature search, research, and data analysis, E. Forzisi Kathera-Ibarra performed FRAP analysis, A. Balatsky prepared/maintained primary neuron cultures and performed Sholl analysis, M. Dubey performed western blotting and primary neuron culture analysis, R. Amin performed behavioral analysis and data analysis (heat maps), S. Venkateswaran performed CHO and N2a cells data analysis, S. Dutto performed immunofluorescence and western blotting, I. Seth performed N2a cells data analysis, A. Ashor performed data analysis and helped with Western blotting, A. Nwandiko performed genotyping and maintained CHO and N2a cells cultures, P. Y. Pan helped with confocal analysis, D. P. Crockett helped with behavioral analysis, tracer analysis, and IF, and F. Sesti directed the study and wrote the manuscript.

Competing interests

The authors declare no competing interests.

Additional information

Supplementary information The online version contains supplementary material available at https://doi.org/10.1038/s42003-024-07344-6.

Correspondence and requests for materials should be addressed to Federico Sesti.

Peer review information *Communications Biology* thanks the anonymous reviewers for their contribution to the peer review of this work. Primary Handling Editor: Rosie Bunton-Stasyshyn.